Acta Materialia 256 (2023) 119142

Contents lists available at ScienceDirect

Acta Materialia

journal homepage: www.elsevier.com/locate/actamat

Twinning induced spatial stress gradients: Local versus global stress states in hexagonal close-packed materials

Herman Fidder [a,b], Indranil Basu [a,c], Jeff Th.M. DeHosson [a,*]

[a] Department of Applied Physics, Zernike Institute for Advanced Materials, University of Groningen, Groningen 9747 AG, the Netherlands
[b] Department of Mechanical Engineering, Cape Peninsula University of Technology, Cape Town, South Africa
[c] Laboratory of Metal Physics and Technology, Department of Materials, ETH Zürich, Zürich 8093, Switzerland

ARTICLE INFO

Keywords:
Twinning
Grain-boundary
Local stress
Dislocations
Hexagonal close-packed materials

ABSTRACT

Length scale dependent microstructural heterogeneities serve as effective pathways in engineering materials for providing simultaneous strength-ductility enhancement. In this regard, hexagonal close-packed (hcp) materials that exhibit a combination of slip and multiple twinning modes potentially act as ideal candidates that generate heterogeneous microstructures. However, such an inhomogeneous distribution of crystallographic defects also results in build-up of spatially heterogeneous local stress gradients that can be distinct from globally applied stress state. In particular, stress fields arising at the vicinity of deformation twins and due to their interaction with grain interfaces often act as precursors to damage nucleation in most hcp metals and alloys. Hence, assessment of such local stresses and their overall impact on plasticity becomes necessary in order to understand the relationship between twinning and fracture in hcp materials. The current work utilizes commercially pure titanium (cp-Ti) as a model material to investigate the impact of twinning induced stress gradients on the local mechanical response. By means of correlative multiscale structural characterization and local stress gradient measurements, we establish a definitive relationship between applied stress vis-à-vis local stress on the local plasticity behavior ahead of a $\{11\overline{2}2\}$ compression twin-grain boundary intersection in cp-Ti. Additionally, the role of twin interfacial structure for tension and compression twinning modes are experimentally determined and their corresponding impact on the local stress fields and associated twin migration mechanisms is assessed.

1. Introduction

Metallic materials play the role of key structural materials addressing the rapidly burgeoning needs of the manufacturing industry, despite the fact that most metallic systems can either display large strengthening or enhanced ductility, but not both at the same time. In this regard, considerable efforts have been made in recent years in designing materials that are able to evade the well-known strength-ductility trade off effect [1–6]. One of the potent means in this direction is by employing material processing routes that involve intelligent tailoring of microstructural heterogeneities across multiple length scales [1,2,4,7–14]. Such a spatial distribution of structural heterogeneities thus generated, results in length scale dependent microstructural constraints. In fact, this approach has proved to play a critical role in altering the mechanical properties of the material, whereby potentially multiscale strengthening and plasticity can be implemented.

An inherent complexity with such multiscale microstructural constraints is the presence of spatially heterogeneous *local stress gradients* that trigger distinct size dependent plasticity mechanisms. Here, the critical issue is that these mechanisms seldom bear correlation with the *globally applied macroscale stress state* [15–19]. In terms of material response, heterogeneous microstructures draw similarities to a composite like behavior, wherein the macroscale plasticity represents the *mean characteristics* arising from the superposition of local scale mechanical response that can vary spatially across the microstructure. Consequently, such spatially dependent fluctuations in stress fields within the microstructure plays a crucial role when determining the preferential zones for local damage nucleation and the overall fracture response in these materials [1,2]. In statistical terminology, we may state that *mean characteristics* described by Gaussian non-correlated events in plasticity on a macroscale cannot be used to describe non-Gaussian correlated local events in structure-property relations. In simpler terms, the deformation occurring locally and stochastically in different regions of the microstructure can commence in a

* Corresponding author.
E-mail address: j.t.m.de.hosson@rug.nl (J.Th.M. DeHosson).

https://doi.org/10.1016/j.actamat.2023.119142
Received 5 March 2023; Received in revised form 29 June 2023; Accepted 3 July 2023
Available online 6 July 2023

non-correlated fashion yet the exhibited macroscale flow stress is typically a mean response of a set of such local events occurring all throughout the microstructure. On the other hand, local correlated deformation events such as plasticity transfer across interfaces may starkly deviate from the macroscale mean plasticity response i.e. described by *non-Gaussian correlated events*, but still are important to consider when understanding plasticity driven failure that largely stochastic and local stress dependent. The description is relevant when correlating deformation response across different length scales in anisotropic materials. For obvious reasons, this is so in particular for polycrystalline hexagonal close packed (hcp) metals and alloys having an intrinsic anisotropy in its crystallographic structure.

Nonetheless, hcp metals and alloys that deform by slip and multiple twinning modes serve as ideal candidates for designing materials with heterogeneous microstructures [9,11,20–22]. However, their successful incorporation into state-of-the-art advanced materials application remains hampered due to their poor ductility response [23–27]. This is attributed to their lower crystal symmetry compared to cubic crystal structures, whereby mechanical processing often results in large microstructural anisotropy due to lack of sufficient deformation modes that can provide uniform strain accommodation along the ⟨a⟩ and ⟨c⟩ axes [25]. The mechanical anisotropy effect is further aggravated by profuse deformation twinning activity that gives rise to directionally dependent shear strain accommodation and is associated with a permanent crystallographic rotation and texture formation [23,25]. Hence, depending on the nature and crystallography of twinning the generated twin-matrix interfaces will lead to distinct local stress fields. Moreover, the interaction of twins with other crystallographic structural defects such as dislocations, grain boundaries further amplify the local stresses, thereby triggering local plasticity mechanisms that deviate from the global deformation response [18,28].

From the perspective of dislocation-dislocation interactions, the aforementioned stresses arise due to mutual interaction of lattice dislocations with dislocations at interfaces (grain/twin boundaries). The fate of the incoming lattice dislocations in terms of being transmitted across, blocked or being absorbed into the interface is often theoretically expressed by the strain transmission parameter m' [29–33], that describes the geometrical compatibility of deformation modes across an interface, in Eq. (1) given as:

$$m' = (\mathbf{n}_{in} \cdot \mathbf{n}_{out}) \times (\mathbf{b}_{in} \cdot \mathbf{b}_{out}) \tag{1}$$

where $\mathbf{n}_{in}$ and $\mathbf{n}_{out}$ are the normalized intersection lines common to the slip planes and the boundary plane and, $\mathbf{b}_{in}$ and $\mathbf{b}_{out}$ are the Burgers vectors of the incoming and outgoing slip systems. Maximizing m' theoretically indicates higher propensity of strain transmission across the interface and consequently an absence of dislocation pile-ups. Similar analogy can be drawn for twin-grain boundary interactions, wherein the probability of twins being transmitted or blocked can be predicted using the strain transmission parameter that depends on the geometrical compatibility between twin planes and shear directions across the interface [32,33]. In such cases, the variables $\mathbf{n}_{in/out}$ and $\mathbf{b}_{in/out}$ associate with the twin plane normal and the twinning shear directions for the incoming and outgoing twin modes [32,33]. Indeed, such a theoretical model provides a predictive tool for describing optimum conditions for transmission under shear of dislocations affecting local strain accommodation but an important aspect is missing. These considerations preclude descriptions and insights in the local stress gradients that strongly dictate non-Gaussian correlated events in local plasticity and fracture mechanisms. This becomes extremely relevant for hcp materials that are prone to plastic anisotropy.

Thus, understanding the mutually exclusive impact of global applied stresses and local stress gradients on the microstructure response in hcp materials becomes critical to assess plasticity mechanisms across multiple length scales, as well as for unraveling the origins of instabilities like void nucleation, crack propagation, and premature failure in such plastically anisotropic systems. In particular, simplistic correlations between the macroscopic stress state and the corresponding local plasticity response based upon the Schmid factor, often implemented for homogeneous microstructures, cannot be universally applied to heterogeneous and anisotropic microstructures like hcp without considering the impact of local stress gradients. For instance, stress gradients arising from twin formation and resultant twin-grain boundary interactions in hcp metals and alloys may potentially act as precursors to localized failure despite a global applied stress that favors plasticity [25,34,35]. Unfortunately, the nature and magnitude of stress fields generated around twin-grain boundary interaction zones and its corresponding impact on micron scale plasticity is not well understood and is subject of prime importance in the current study.

Moreover, the dependency of the twinning related stress fields on the mode of twinning is another aspect that still needs to be explored more deeply. It is well established that hcp metals exhibit distinct twinning modes depending on the loading sense along the c-axis i.e. under tension or compression mode [23,26]. In relation to the loading mode, twinning under c-axis extension is commonly denoted as *tension* twinning, whereas twins forming under c-axis compression are addressed as *compression* twins [9,23,25,36]. It must be noted in selected works [37–39], these twins are also referred to as *extension* and *contraction* twins. While the former nomenclature is associated with the nature of applied stress, the latter naming convention describes the sign of imposed strain along c-axis. Although, both naming conventions are largely accepted in the literature, in the present work, the twinning modes will be referred with respect to the nature of applied stress i.e. *tension* vs. *compression*. The corresponding stress to nucleate and propagate twins formed under c-axis tension vis-à-vis c-axis compression is known to differ starkly, with the latter mode typically requiring significantly higher stresses [23,25,36,40,41]. In addition, the twin-boundary migration mechanisms in hcp materials are uniquely depending on the mode of twinning, as tension twins are known to grow primarily by atomic shuffling [42–44] whereas compression twins mostly involve shear driven motion of twinning partials and display rather low activity of shuffling [45–48]. For instance, $\{10\bar{1}1\}$ twins migrate solely by motion of twinning dislocations [46,48], while numerous competing theories that are reported on the mechanistic of migration of $\{11\bar{2}2\}$ twin boundaries either involve a combination shear and shuffle [45] or via. pure glide of twinning dislocations [47]. Important to realize that this is unlike twin propagation in cubic crystals that are typically described by the conservative motion of a set of two partials that enclose a twin fault [49]. In light of these considerations, hence the second aspect of the current work is to scrutinize the role of the twin interfacial structure for different twinning modes on the resultant local stress fields that develop around them, and their subsequent impact on the local strain accommodation mechanisms.

With regard to the experimental approach, in an earlier work [28], the authors probed into the spatial stress gradients that develop ahead of a $\{10\bar{1}2\}$ tension twin-grain boundary intersection as well as stress fields lateral to a $\{10\bar{1}2\}$ tension twin in commercially pure titanium (cp-Ti) microstructure. It was concluded that the in-twin stress fields impact plasticity within the twinned region in terms of promoting secondary twinning or de-twinning response. The current work extends our understanding to compression twins that are often associated with much larger nucleation and migration stresses. Moreover, compression twinning induced stress fields, as is often regarded as a precursor to premature failure in hcp metals and alloys becomes critical to quantify in order to address the overarching issue of the relationship between twinning and fracture in hcp materials.

By means of correlative multiscale structural characterization and local stress gradient experimental measurements, the present work sheds new light by establishing a definitive relationship between *globally applied stress* vis-à-vis *local stress* on the local plasticity behavior ahead of a $\{11\bar{2}2\}$ compression twin-grain boundary intersection in cp-Ti.

Orientation imaging microscopy by means of standard electron backscatter diffraction is utilized to assess the impact of loading response on the grain-level mesoscale deformation. By means of Schmid factor analysis and strain transmission evaluation the plasticity response of Ti-grains is evaluated under applied uniaxial tension. Concurrently, the local sub-micron scale deformation is probed by determining local stress gradients near the twin-grain boundary interface and related plasticity mechanisms are identified by appropriate nanoscale microstructural characterization using transmission electron microscopy and transmission Kikuchi diffraction techniques. The observations show stark deviations in plasticity mechanisms arising from the globally applied stress and local stress gradients. Additionally, the role of twin interfacial structures for tension and compression twinning modes are experimentally determined and its corresponding impact on the local stress fields is assessed. The findings are discussed in a quantitative manner within the framework of the twinning mode dependent migration mechanisms, and the associated stresses.

2. Experimental methods

2.1. Mechanical testing and characterization using conventional SEM/EBSD

Commercially available grade II titanium was homogenized at 830 °C for 120 mins. Tensile dog-bone specimens, machined with gage dimensions of 32 mm × 6 mm × 3.2 mm (ISO 7500–1), were cryogenically cooled down by dipping in liquid nitrogen. The cryogenic tensile coupons were subsequently strained under uniaxial tension at an applied strain rate of $10^{-2}s^{-1}$ upto a final strain of 2%. It must be mentioned here, that deformation tests were performed at low temperatures around 100 K to promote twinning-mediated plasticity, which typically associates with large mechanical anisotropy and heterogeneous stress gradients. Moreover, despite the deformation being performed under uniaxial tension, the impact of the applied stress will strongly depend upon the orientation of the grains such that those with their c-axes oriented perpendicular to the loading axis will prefer to twin under compression, while those having their c-axes aligned with the tensile direction will tend to undergo tension twinning. The tensile-test specimens were polished prior to deformation and the selected region of interest was marked using a grid of micro indents. The UTS is found approximately 312 MPa and yielding at 208 MPa. The average size of the equiaxed grains was approximately 250 to 300 micrometer.

Electron-backscattered diffraction (EBSD) was performed for microstructural characterization which produced both orientation and topographical orientation information of each individual grains. EBSD measurements were made using a Tescan Lyra dual beam FEG-SEM/FIB (Field-Emission-Gun Scanning Electron Microscope/Focused Ion-Beam) equipped with an EDAX TSL EBSD system with Hikari Super CCD camera used for acquiring EBSD patterns. An electron beam accelerating voltage of 25 kV and current of 20 nA was used. A step size of 0.3 μm and hexagonal type of grid was used for collection of EBSD data. A binning width of 4 × 4 was used for collection of Kikuchi patterns using 640 × 480 CCD camera resolution. EDAX-TSL OIM™ Analysis was used to analyze the acquired raw EBSD data (software and MTEX open source Matlab toolbox) [50]. A scanning electron microscope (SEM) was used to image the slip traces in each individual grain. Focused ion beam milling was used to mill into the region containing the grain boundary plane of which the orientation was determined by examining the boundary trace along the milled cross-section. Microstructural observation was made with the direction of viewing parallel to the surface normal (referred to as ND), on the dog-bone tensile coupons.

2.2. Residual stress measurements using FIB-DIC milling

The method used in this study is essentially based on combining electron-imaging techniques of a dual beam (electrons and ions) scanning microscope. An initial secondary electron image is recorded, after which a slit is milled on the surface using the focused ion-beam. This is followed by a second secondary electron image of the same area. It must be mentioned that both electron and ion-beam column have different orientations, which means that the specimen is repositioned for milling. Comparing the first and second SEM images, a before and after stress release displacements by the digital image correlation (DIC) software are obtained. These displacements are compared with those obtained by the analytical solution (Eq. (2)), and the value of residual stress perpendicular to the plane of the slit is obtained from the slope of the fitting [51,52],

$$U_{dir} = \frac{2.243}{E'}\sigma_{dir}\int_0^a cos\theta\left(1+\frac{sin^2\theta}{2(1-\nu)}\right)\times(1.12+0.18\cdot\mathrm{sech}(tan\theta))dz \tag{2}$$

where E' is $E/(1-\nu^2)$, E is the Young's modulus, ν is the Poisson's ratio, θ is $arctan(d/a)$, a is the depth of the slit and d is the distance from the slit; $'dir'$ represents x or y directions. The displacements caused by the stress release depend on the slit depth a and are directly proportional to σ/E ratio.

The DIC software (GOM Correlate v. 2016) processes the before and after SEM images, by subsequent displacements adjacent to the slit for each facet (group of pixels) position. A typical DIC contour map is shown in Fig. 1, which exemplifies the relative displacements normal to the milled slit that corresponds to the local stress release. Important to note is the range of the scale bar of the image that is of tens of nanometers. The DIC data was post-processed using a Matlab based script [15,28] in order to determine the residual stress values from the experimentally measured displacements. A linear slit, oriented normal to the grain boundary trace, with a width of 0.5 μm, depth of 2.5 μm, and length of 40 μm was milled in the area of interest (c.f. Fig. 2a). In order to ensure a high spatial resolution of the measured displacement field, multiple high magnification (field of view of 10 μm) SEM images of resolution 768×768 pixels were obtained. Facet sizes of 19×19 pixels were used for DIC software input with a step width of 16 pixels. The surface was decorated by Yttria-stabilized Zirconia (YSZ) nano-particles to obtain optimum image contrast for high accuracy DIC analysis (see Fig. 2a, 2b and 2c).

The authors used the same measurement technique as previously published and for details reference is made to [15,52] to quantify the stress release displacement of the materials in the range of nanometers. In order to calculate the stresses an accurate estimate of the slit depth is required that is given in Fig. 2d. In the present work SEM imaging parameters were optimized as per [52,53] to minimize experimental drift related inaccuracies.

A multiple fitting approach [15,52], wherein a stress value is obtained for displacements corresponding to each row used in the DIC analysis and analyzed separately was implemented to account for spatially heterogeneous stress states. In essence, this new method gathers information not only from averaged data of one slit milled, but also for each line in the slit, which leads to a better lateral resolution. It is shown in Ref. [52] that indeed this approach enhances the lateral resolution and allows details about local stress state at the sub-micron scale, in particular relevant when stress gradients are present. It must be noted that the elastic stiffness in hcp materials fluctuates based on the loading direction with respect to the c-axis i.e. compressive loading parallel to c-axis corresponds to a *crystallographically hard orientation* and is associated with higher elastic modulus compared to loading perpendicular to c-axis that conforms to a *crystallographically soft orientation*. Hence, the stress calculations were made using orientation dependent

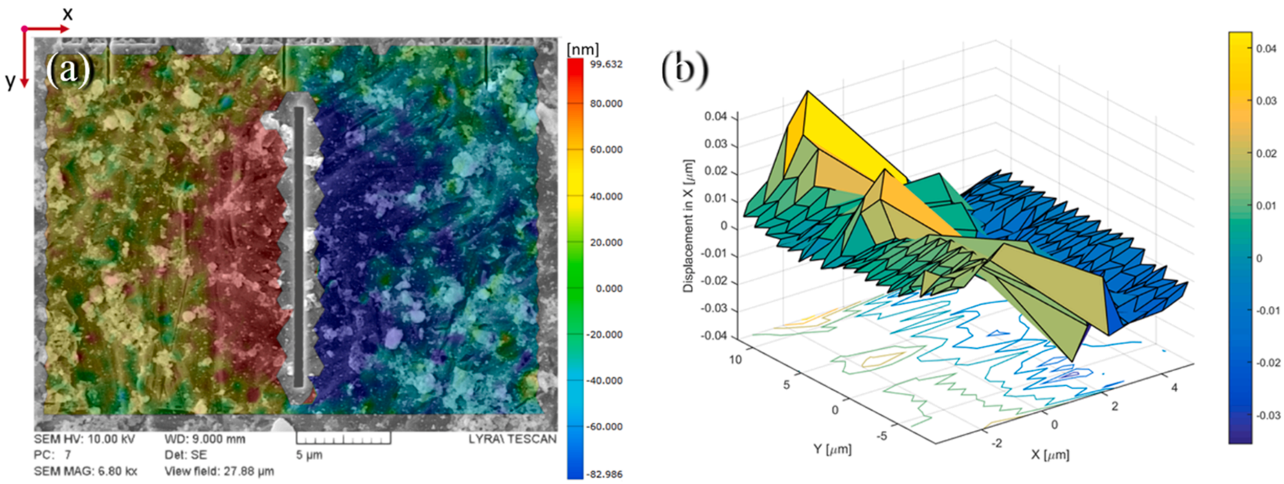

Fig. 1. (a) Typical displacement map obtained from the DIC software for a surface under homogeneous stress, red color indicates positive displacements along the x-axis (perpendicular to the slit length) and blue color refers to negative displacements (b) Corresponding MATLAB processed surface plot of the displacements illustrating large positive and negative displacements at the vicinity of the slit.

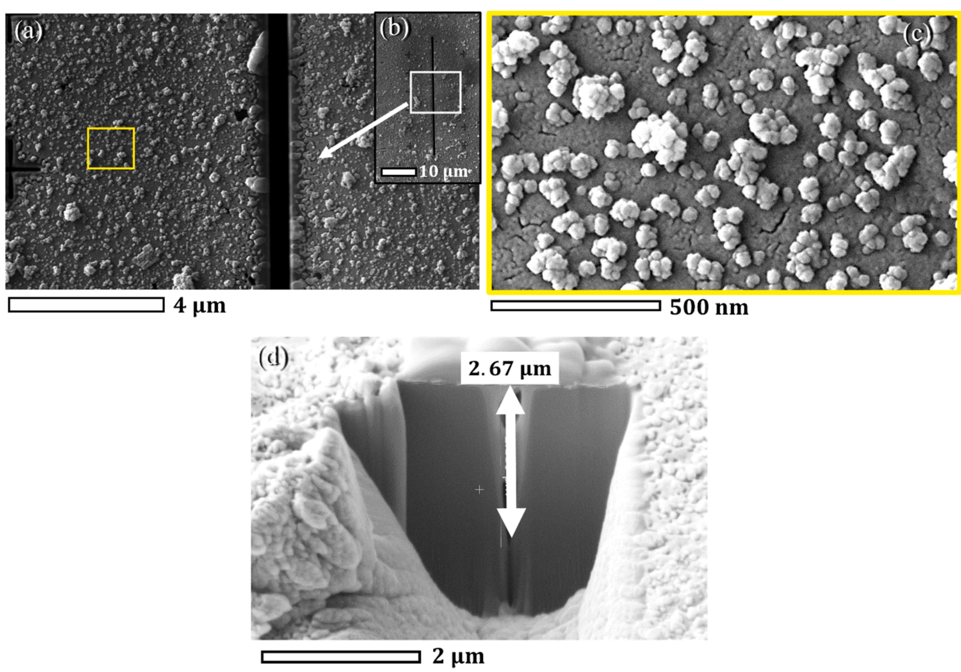

Fig. 2. (a) Nano-scale surface patterning using yttria stabilized zirconia (YSZ) nano-particles, (b) inset image showing the milled slit in cp-Ti, (c) magnified view of the surface showing the fine dispersion of YSZ nano-particles and (d) slit depth determination by FIB cross-section milling.

elastic modulus values, extracted from Ref. [54], wherein the angle between the loading axis and the crystal c-axis was varied to obtain an angular dependence of the elastic modulus with respect to c-axis orientation.

2.3. Transmission EBSD measurements in scanning electron microscopy (t-EBSD) and transmission electron microscopy (TEM)

Transmission electron-backscatter diffraction / transmission Kikuchi diffraction (t-EBSD/TKD) inside an SEM sounds a bit peculiar but it combines the detection of Kikuchi bands of forward scattered electrons with the scanning possibilities of the scanning electron microscope (SEM). In practice, there are only two demanding conditions: the first is that the specimen is thin enough for the transmission of electrons with energies typical in SEM, not TEM. The optimum thickness is obtained when the specimen is thick enough to scatter the electrons towards the detector, but still thin enough not to significantly backscatter and absorb the incident electron beam. The second demand is tilting possibilities in the opposite direction to conventional EBSD-SEM operations. The lateral resolution has been shown to change as a function of tilting angle and specimen thickness. In general, the thinner the specimen, the better the spatial resolution. For details and explanations see Ref. [55].

Specimens for transmission EBSD (t-EBSD) and transmission electron microscopy (TEM) measurements was prepared using standard lift-out techniques from the region of interest in the bulk material inside a dual beam FIB-SEM (FEI Helios 600i) using a micro-manipulator needle (as illustrated in Fig. 3a and 3b). The cross-sections were thinned down to electron transparency with stepwise lowering of the milling voltage and current, such that the final polishing step is performed at 2 kV for a milling current of 10 pA (Fig. 3c). t-EBSD measurements were performed

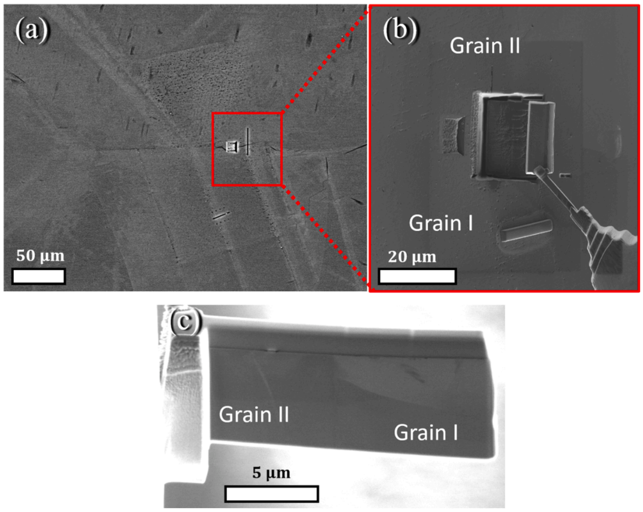

Fig. 3. (a) Site-specific FIB liftout performed at twin-grain boundary interaction region, (b) lamella liftout using a micro-manipulator needle and (c) FIB lamella glued to the TEM half-grid prior to final thinning procedure.

in the FEI Quanta 200 FEG-SEM at an accelerating voltage of 30 kV and beam spot size of 4 nm. The specimen was tilted at an angle of −5° A step size of 10 nm and a hexagonal type of grid was implemented. Like in the Tescan Lyra dual beam SEM set-up, a binning of 4 × 4 was used when capturing the Kikuchi patterns, producing a 640×480 CCD camera resolution. In order to achieve very high indexing rates, the raw unfiltered t-EBSD/TKD data was re-indexed employing a neighborhood pattern averaging (n-PAR) scheme to improve the pattern signal to noise ratio [56]. The n-PAR algorithm is available as a built-in function in the conventional EBSD analysis software OIM™ Analysis 8 [47] Noise filtering was performed with a threshold confidence interval of 0.2.

Low kV STEM imaging on the t-EBSD lamella was performed in an FEI Helios 600i SEM, operated at 30 kV with current of 0.17nA. The advantage of low kV STEM lies in better surface contrast imaging [57]. TEM imaging and dislocation analysis on the lamella was additionally performed on the lamella in an FEI Talos™ F200X microscope operated at 200 kV.

3. Results

3.1. Mesoscale structural characterization using conventional EBSD

Fig. 4a and 4b present the inverse pole figure (IPF) orientation maps of the commercially pure Ti before and after tensile test. Deformation up to 2% strain resulted in appearance of compression twins within grains oriented with their c-axes perpendicular to the tensile direction (TD). The direction of applied uniaxial tension is shown in Fig. 4a. The compression twins are identified as $\{11\bar{2}2\}$ twins described by an angular misorientation of 64.3° about the $\langle\bar{1}100\rangle$ axis. Fig. 4c and 4d present the IPF orientation and kernel average misorientation (KAM) maps of the twin-grain boundary intersection zone highlighted in Fig. 3b. KAM provides information on a local level about the misorientation with respect to the crystal orientation at the center of the kernel. KAM values are plotted with a threshold angle of 2° using the 2nd nearest neighbor [3,6,15,28]. The region subjected to local residual stress measurements by milling a linear slit is schematically illustrated in Fig. 4c. Fig. 4d indicates a concentration of strain at the twin-grain boundary intersection region that extends into the neighboring grain. Fig. 4e shows a magnified SEM image of the twin-grain boundary intersection. The twin upon hitting the grain boundary induces a shear-coupled migration of the interface. The magnitude of grain boundary shear is measured as 0.45, which corresponds to two times the

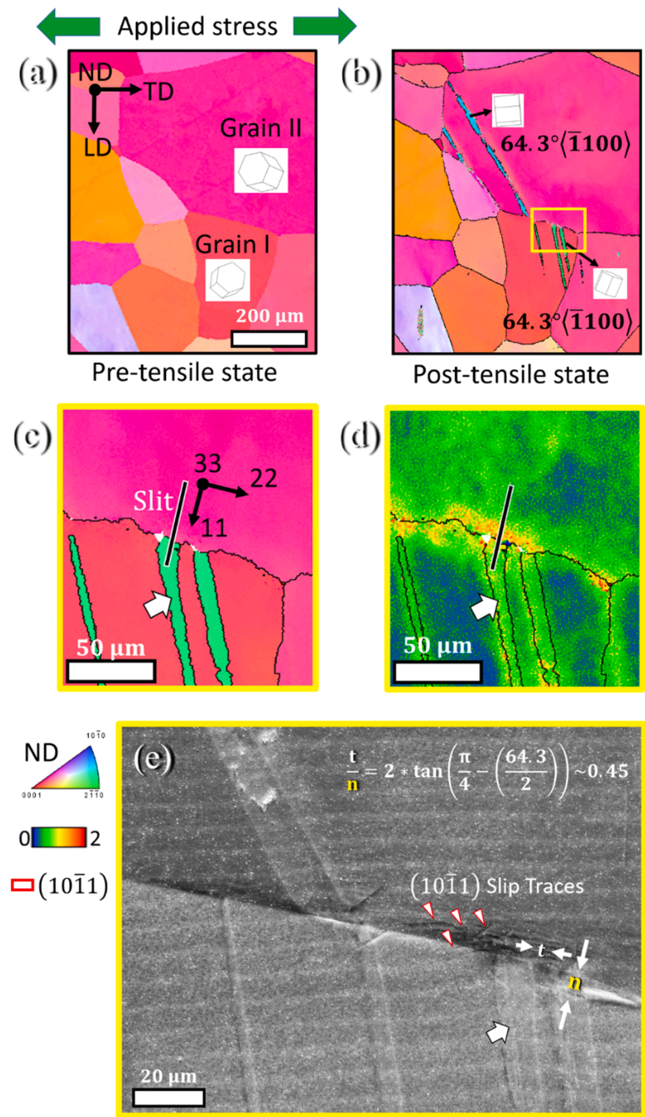

Fig. 4. Inverse-pole figure (IPF) maps of the region of interest (a) before and (b) after tensile test. Applied stress and the global coordinate system is indicated in (a). Orientations of grains and twins are additionally shown by crystal unit cells. The region of interest corresponds to the Twin I and Grain II interaction zone. (c) Slit location with respect to the microstructure and corresponding local slit coordinate system, (d) Kernel average misorientation (KAM) map of the region in the vicinity of the slit and (e) magnified SEM image of the Twin I-Grain II interface, the impinging twin induces local grain boundary shearing associated with the presence of pyramidal slip traces (shown in red outlined white arrowheads) in the neighborhood. The IPF color-coded stereographic triangle is shown corresponding to the images in (a), (b) and (c) is shown. RGB color-coding highlighting KAM misorientation values ranging from 0° to 2° additionally depicted.

shear resulting from $\{11\bar{2}2\}$ compression twin ($\gamma_{\{11\bar{2}2\}} = 0.22$) [26]. The SEM image additionally indicates slip traces ahead of the twin-boundary intersection that correspond to the $\{10\bar{1}1\}$ pyramidal planes.

3.2. Dislocation density and spatially resolved stress gradients at compression twin-grain boundary interaction zone

The density of geometrically necessary dislocations (GND density, ρ_{GND}) values from standard EBSD data in Fig. 4 were calculated using the strain gradient approach [58,59], given by the expression in Eq. (3):

$$\rho_{GND} = \frac{2\theta}{q\lambda b} \tag{3}$$

where θ is the experimentally measured KAM value obtained from Fig. 4d, λ is the step size, q is the number of nearest neighbors averaged in the KAM calculation, and b is the magnitude of the Burgers vector corresponding to the active slip system in the grain, in the present case it corresponds to $\langle a \rangle$-type dislocation slip. Fig. 5 presents the experimentally measured geometrically necessary dislocation densities across the compression twin-grain boundary intersection plane. Fig. 5a shows the misorientation gradient along with the GND density on the adjacent sides of the twin-boundary interface. The values indicate an order of magnitude difference in the dislocation density at the interface vis-à-vis the interior of grain II. Within the twin, the relative decrement in dislocation density is by a factor of ~2 compared to the dislocation density measured at the interface. The point to origin misorientation values mimic the trends exhibited by the dislocation density gradient. The corresponding measured residual stresses is presented in Fig. 5b. The inset image (c.f. Fig. 5c) shows the geometry of the slit with respect to the compression twin-boundary interface. The stress values are measured along the direction lateral to the slit length and in the current case acting along the interface between Twin I and Grain II i.e., σ_{22} as drawn in Fig. 4c. In order to estimate the Twin I and Grain II reference stress states, the measured stress values ($\sigma_{meas.}$) is expressed as a function of one over square root of the distance (d_{gb}) from the interface assuming the classical Hall-Petch relationship [60–62] given as,

$$\sigma_{meas.} = \sigma_{ref} + \frac{k_{HP}}{\sqrt{d_{gb}}} \tag{4}$$

where, σ_{ref} refers to reference stress state in the grain bulk and k_{HP} is the Hall-Petch coefficient or obstacle strength. In the present case, the reference stress values refer to the 22 direction, i.e., the direction lateral to the slit length.

The Hall-Petch model [60,61] in Eq. (4) derives from the Eshelby-Frank-Nabarro formulation [63] of pile-up due to a linear array of dislocations showing that the stress values scale inversely over the square root of distance between the tip of the pile-up and dislocation source. The former model can be additionally extended to describe strengthening in polycrystalline materials based on local dislocation

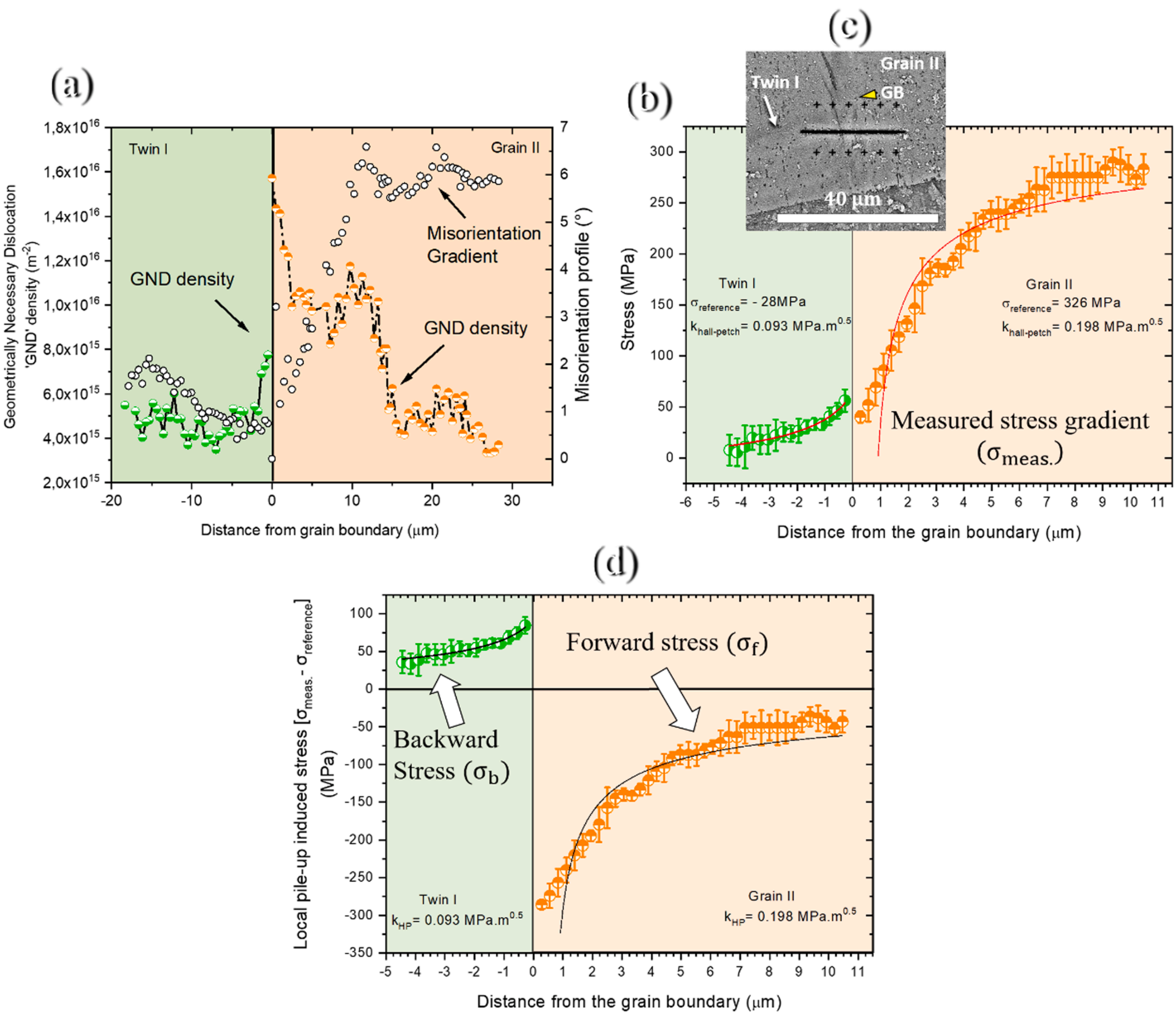

Fig. 5. (a) Point-to-Origin Misorientation profile (with origin located at the twin-grain boundary interface) and geometrically necessary dislocation (GND) density gradients, corresponding to $\langle a \rangle$- dislocations, calculated across the Twin I-Grain II interface. Peak GND density measured at the interface as 1.6×10^{16} m^{-2}; (b) Measured residual stress profile along direction *22* across the Twin I-Grain II interface, empirical fitting to Hall-Petch dependency gives the grain reference stress for Twin I as −28 MPa and Grain II as 314 MPa. (c) Plot showing the twin-boundary interaction induced stress gradients calculated by stress differential between the measured residual stress (σ_{meas}) and reference stress (σ_{ref}).

pile-up phenomenon. This is done by assuming the pile-up length to be half of the mean grain diameter for polycrystalline aggregates i.e. $L_p = d_{gb}/2$. Theoretically, the Hall-Petch coefficient, k_{HP} equates to $\sqrt{\alpha Gb\tau_{cr}}$, where α represent a hardening coefficient connected to geometry of dislocation-dislocation interaction often close to 0.5, Gb is the product of shear modulus and Burgers vector. τ_{cr} is the critical pile-up stress after which the grain boundary resistance yields to incoming pile-up. The variable k_{HP} thus essentially describes the individual grain-boundary obstacle-strength. In this particular case, the fitted coefficients are derived from quantitative estimates of local stress gradients calculated by FIB-DIC milling technique across a specific twin-grain boundary interface and describe the local grain boundary resistance to incoming dislocation slip. The implications of these values in context to obstacle-strength will be discussed later on in the text.

As per Eq. (4), Grain II in Fig. 5b exhibits a tensile reference stress value of 326 MPa, with the absolute stress values dropping sharply on moving closer to the interface, thereby indicating a strong compressive local stress state in front of the twin-boundary intersection existing in grain II. In case of the twin, while the local stress near the interface is tensile in nature, the reference stress state of the twin is compressive and estimated as −28 MPa. Another critical observation pertains to the mismatch in stress values across the interface in twin I vis-à-vis grain II. The stress differential between the measured stress value near the interface and the reference stress state of the grain gives the contribution of twin-grain boundary interaction stress. This is determined along the direction *22* in Grain II to be −286 MPa (forward stress contribution, σ_f). Similarly, the local stress due to twin-grain boundary interface exerted within twin I is obtained as 88 MPa (backward stress contribution, σ_b). Fig. 5b also indicates the k_{HP} values or the *dislocation locking parameter* [49] for twin I and grain II as 0.093 $MPa\sqrt{m}$ and 0.198 $MPa\sqrt{m}$, respectively. In order to illustrate the stress gradients solely arising due to the Twin I - Grain II interface, Fig. 5d shows the forward stress gradients within Grain II and the backward stress gradients within Twin I. As regards to the details of the fitting procedure, it is noteworthy that the back stress gradients in Fig. 5d do not look asymptotic at a distance to the boundary $d = 0$, where the stress should tend to go to infinity. This is owing to the uncertainties that arise with the fitting procedure, wherein grain boundary positional uncertainty and an uncertainty in the far field stress (that should ideally be zero) needs to be considered [64]. Regarding the former, a positional error for the grain boundary (as introduced in Ref. [64]) of 1 micrometer is assumed accounting for the grain boundary plane inclination (see Figs. 6 and 7) whereby the normal distance (from the pile up source to the grain boundary) will vary as a function of the depth. The latter uncertainty correlates to a non-zero reference stress in real cases and is represented by the σ_{ref} values that are calculated above.

Fig. 6a shows an SEM image of region comprising the milled slit. Cross-section mill of the region enclosing the grain boundary plane indicates the orientation of the grain boundary plane to be nearly perpendicular to the slit length, shown in Fig. 6b and 6c. Additionally, there are appearance of cracks propagating along the grain boundary as indicated in Fig. 6a and in the cross-sectional view in Fig. 6c (see green arrows). The cracks appear to be associated with twinning activity within grain II, indicated by red arrows in Fig. 6c.

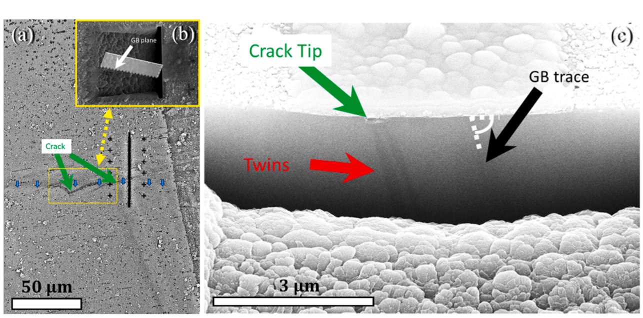

Fig. 6. (a) SEM image showing appearance of cracks along the grain boundary trace near the Twin I-Grain II interaction zone, (b) inset image shows the orientation of the grain boundary plane between Twin I- Grain II; c) Cracks associated with fine twins in grain II, grain boundary plane trace additionally indicated by white dotted line.

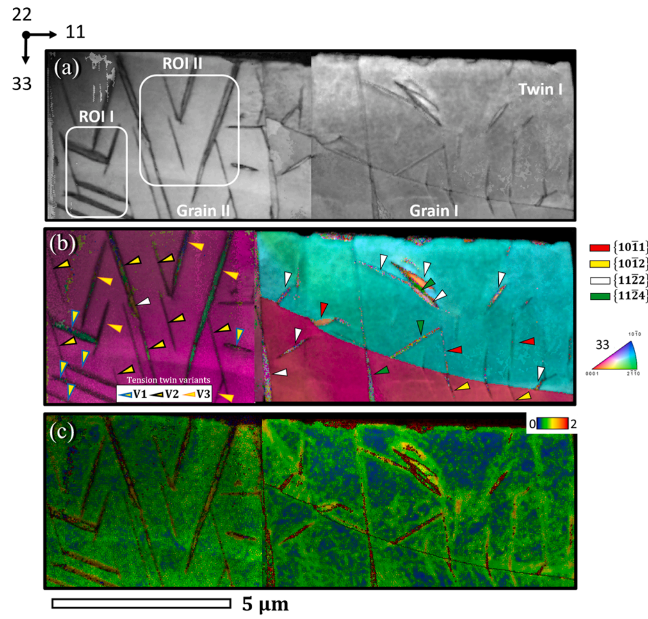

Fig. 7. t-EBSD measurements on the lamella containing the twin-grain boundary interface (shown in Fig. 3c). (a) Image quality map showing a high density of twins in Grain II and formation of second order twins within Twin I. (b) IPF map of the same region; yellow arrowheads indicate $\{10\bar{1}2\}$ tension twins, red arrowheads indicate $\{10\bar{1}1\}$ compression twins, white arrowheads indicate $\{11\bar{2}2\}$ compression twins and green arrowheads show the $\{11\bar{2}4\}$ compression twins. Different $\{10\bar{1}2\}$ twin variants shown by yellow arrowheads with blue (V1), black (V2) and red (V3) borders, respectively. (c) Corresponding KAM map of the region shown in (a).

3.3. Nanoscale structural characterization using t-EBSD

Fig. 7 presents nanoscale characterization of the region comprising the $\{11\bar{2}2\}$ compression twin-grain boundary intersection zone by means of t-EBSD. Fig. 7a shows the image quality map, indicating a high density of nanoscale twins nucleating within grain II, as well as twins forming inside twin I. Additionally, the presence of twins that nucleated at the twin I - grain I interface is also observed. Fig. 7b presents the IPF orientation map wherein the twins are identified by differently colored arrowheads, where each color corresponds to a twin type. In grain II, majority of the twins nucleated correspond to tensile twins with only one compression twin type identified. The nucleated tension twins indicated the presence of three different twin variants marked as V1, V2 and V3 (indicated by yellow arrowheads with blue, black and red outlines in Fig. 7b). Within the large twin (Twin I), secondary twins appear, all of them pertaining to compression twin, while few tension twins nucleate within the matrix (grain I) at the twin I-grain I interface. Fig. 7c represents the KAM map indicating a concentration of strain near the nanoscale twins as well as within twin I, at the vicinity of the twin I – grain II interface.

Fig. 8 presents the single orientation scatter plots highlighting each tension twin variant identified within Grain II. Single orientation scatter pole figures are plotted for, (0002), $(10\bar{1}0)$ and $(11\bar{2}0)$ crystallographic planes. Twin variant V1 indicates a spread around the exact twin orientation (shown in the (0002) pole figure) indicative of substantial slip within the twin and distortion of the original parent-twin

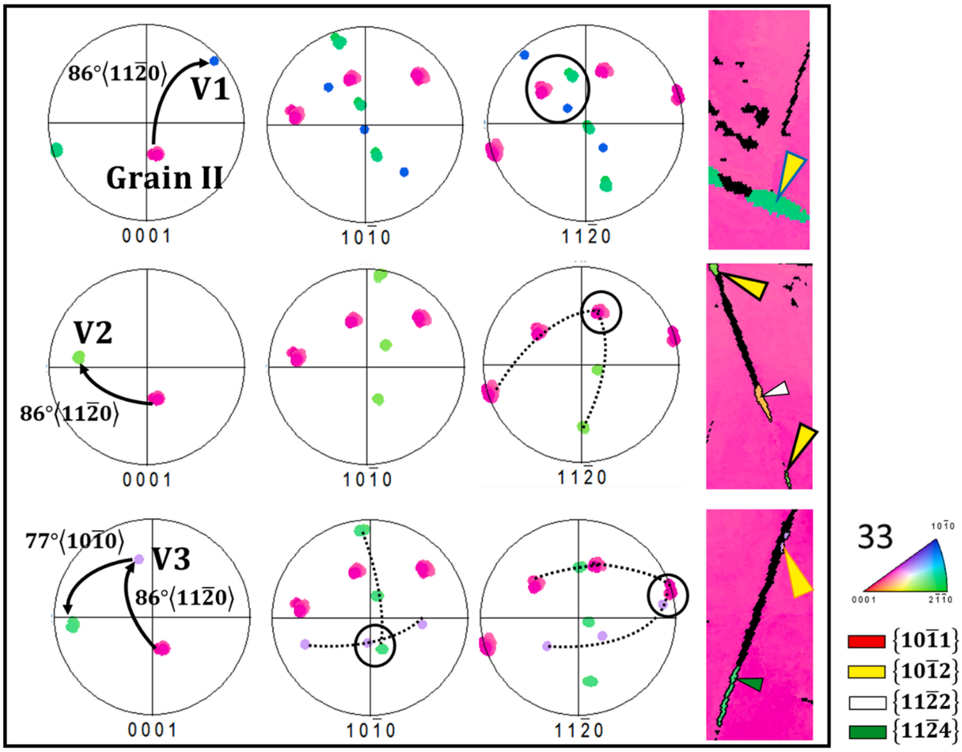

Fig. 8. Single orientation scatter data and corresponding IPF maps showing different {10$\bar{1}$2} twin variants observed in grain II. The shared rotation axis is additionally indicated. Certain twin variants also undergo secondary twinning and corresponding orientations are shown in single orientation scatter data.

relationship, whereby the misorientation axis deviates from the original ⟨11$\bar{2}$0⟩ axis. This is shown by an absence of overlap of the parent and twin orientations in the (11$\bar{2}$0) pole figure, suggesting a slip induced grain rotation, within the twin, about the c-axis. Such loss of twin coherency is attributed to the additional strain imposed from twin-twin interactions as seen from the IQ map in Fig. 7a. Twin variant V2 retains its coherency as indicated by a shared rotation axis in the (11$\bar{2}$0) pole figure. The third variant, V3, is described by the partially indexed purple colored twin orientation that further undergoes secondary {11$\bar{2}$4} compression twinning (shown in light green) as indicated by the shared misorientation axis in the (10$\bar{1}$0) pole figure. Fig. 8 indicates a lack of variant selection observed in the tension twinning response that likely stems from complex interactions between the twinning induced accommodation stresses and the local {11$\bar{2}$2} twin-grain boundary stress fields.

In order to investigate higher order twinning events within the tension twins that formed in grain II, high resolution maps of selected regions encompassing different twin variants are shown in Fig. 9. Fig. 9a and 9b correspond to regions enclosed as *ROI I* and *ROI II* in Fig. 7a, respectively. The IPF map in Fig. 9a indicates the formation of {10$\bar{1}$1} compression twins within the V3 variant. The KAM map indicates the local strain accumulation primary at the interfaces between the secondary and primary twins as well as at the twin-matrix boundary. Fig. 9b indicates the appearance of both {10$\bar{1}$1} and {11$\bar{2}$4} compression twins within the tension twin variant V2. On the other hand, {10$\bar{1}$2} twin variant V3, gave rise to second order {11$\bar{2}$4} compression twinning. KAM values indicate strain concentration at the interfaces of the primary and secondary twins.

3.4. Defect characterization using STEM and TEM

Fig. 10 shows images acquired in STEM mode of the {11$\bar{2}$2} compression twin-grain boundary region. Fig. 10a shows a low magnification image of the lamella, highlighted by high density of twins that

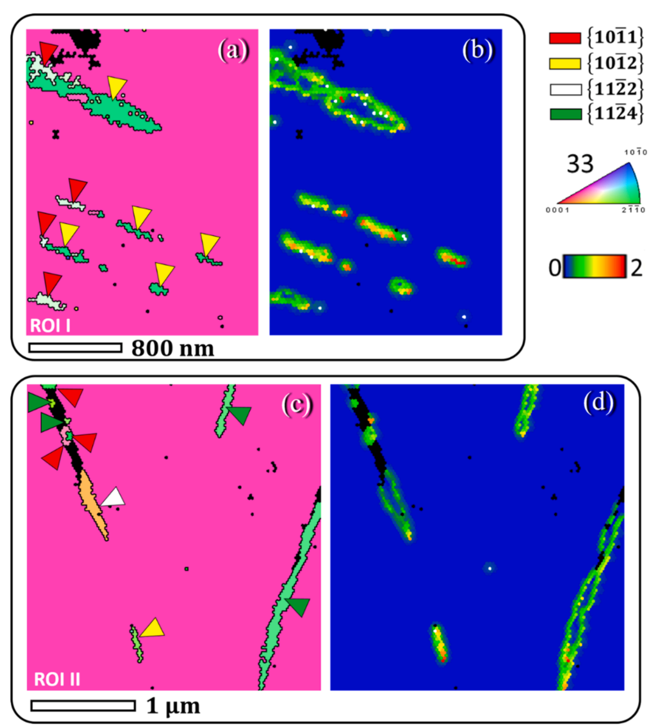

Fig. 9. Magnified view of two region of interests highlighted in Fig. 7a viz. ROI I and ROI II that undergo higher order twinning events are shown. (a) and (b) show the IPF and KAM maps corresponding to ROI 1; (c) and (d) show the IPF and KAM maps corresponding to ROI II. Yellow arrowheads indicate {10$\bar{1}$2} tension twins, red arrowheads indicate {10$\bar{1}$1} compression twins, white arrowheads indicate {11$\bar{2}$2} compression twins and green arrowheads show the {11$\bar{2}$4} compression twins.

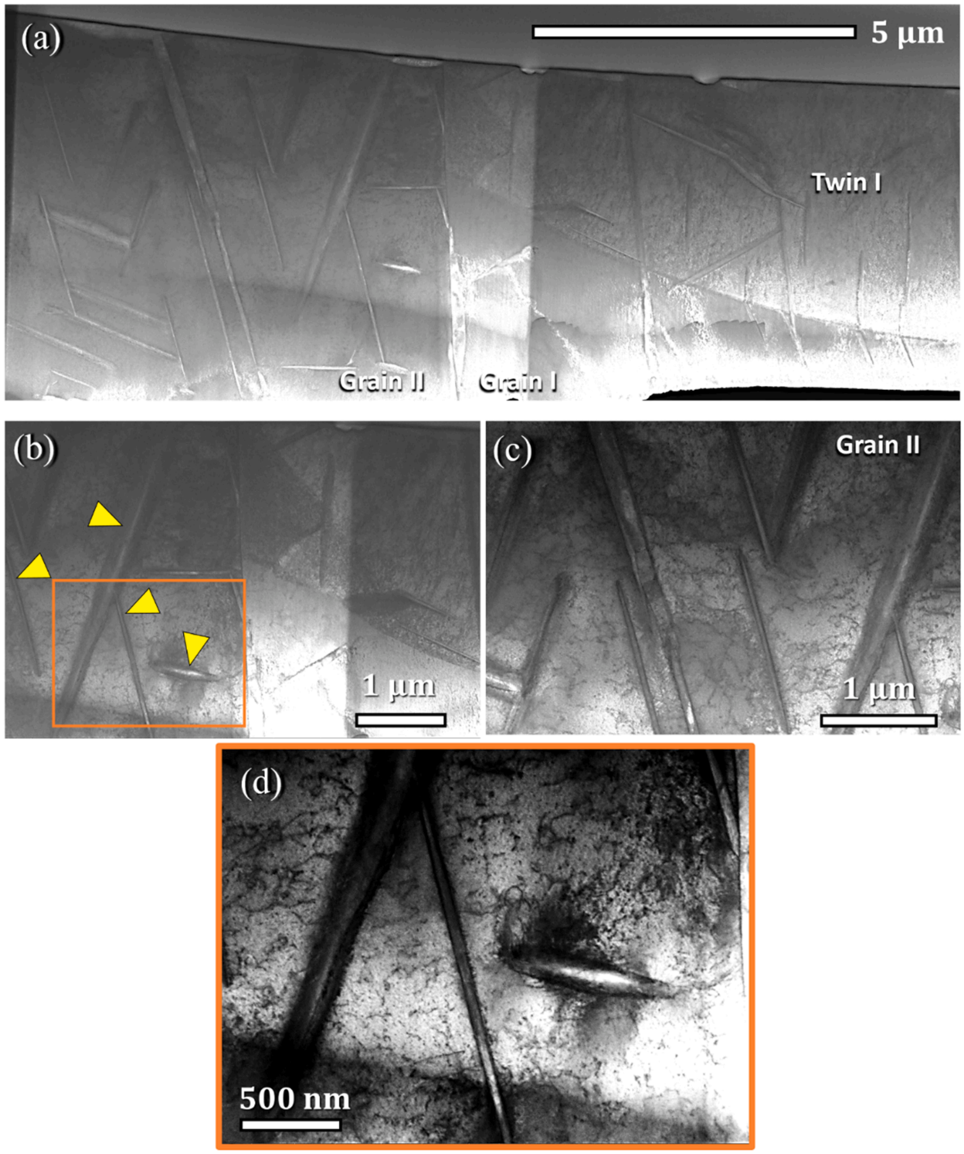

Fig. 10. (a) Low kV STEM imaging of the entire lamella, (b) and (c) show magnified view of the twin-grain boundary interface and tension twins formed within Grain II. Large dislocation pile-up observed within Twin I near the twin-grain boundary interface. Highlighted region in orange in (b) is magnified in (d) to indicate the dense dislocation network surrounding the nanoscale twins. Yellow arrowheads indicate $\{10\bar{1}2\}$ tension twins.

are present, both within grain II and the impinging $\{11\bar{2}2\}$ compression twin (Twin I). The twins are associated with dislocation activity. Fig. 10b and 10c show magnified images of regions corresponding to the grain II-twin I interface and twins within grain II, respectively. Fig. 10b indicates a substantial increase in the dislocation density within twin 1, at the vicinity of the interface. Additionally, significant dislocation activity is preferentially observed near twin tips and at twin-twin intersections, as shown in Fig. 10b and 10c. The region highlighted in Fig. 10b is enlarged in Fig. 10d, representing the defect distribution at the vicinity of a twin and is described by a substantial increment in dislocation density and dislocation-dislocation entanglement.

For dislocation character analysis, TEM images were acquired at higher magnification under the diffraction condition of $\mathbf{g} = 0002$ and $\mathbf{g} = 10\bar{1}0$. Fig. 11a shows a bright field image of dislocation structures in front of a tension twin tip and at the vicinity of the twin formed within grain II, near the twin I-grain II interface. The imaging is performed at $\boldsymbol{g} = 10\bar{1}0$, whereby $\mathbf{g}{\cdot}\mathbf{b}$ analysis would imply selective visibility of all dislocations with an $\langle \mathbf{a} \rangle$ character. The region within the matrix near the twin, highlighted by an orange box (c.f. Fig. 11a), is shown in Fig. 11b with the imaging performed at $\mathbf{g} = 0002$, wherein the dislocations visible correspond to those having a $\langle \mathbf{c} \rangle$ character (see white arrowheads with red outline). The (0002) basal plane trace orientation is additionally depicted by white lines in Fig. 11a and 11b. Comparing both images (Fig. 11a and 11b) it is concluded that while the dislocation segments aligned parallel to the basal trace correspond to $\langle \mathbf{a} \rangle$-type dislocations lying on the basal plane, whereas the inclined dislocations that are lying out of the basal plane either belong to $\langle \mathbf{a} \rangle$-type or $\langle \boldsymbol{c} + \boldsymbol{a} \rangle$-type. Fig. 11c imaged at $\mathbf{g} = 0002$, shows a dark-field (DF) image of the twin tip highlighted in yellow in Fig. 11a. DF imaging provides a better dislocation contrast, revealing the dense dislocation network ahead of the twin, with $\langle \mathbf{c} \rangle$-type edge dislocations piling up on the basal and prismatic planes as indicated by white and orange arrowheads in the inset image. Fig. 11d shows a magnified image of the region marked in orange within the matrix in Fig. 11a indicating a wavy morphology of the inclined $\langle \boldsymbol{c} + \boldsymbol{a} \rangle$ dislocations. Dislocation character analysis on the images in Fig. 11a, 11b and 11d allude to a mixed (edge + screw) character for $\langle \boldsymbol{c} + \boldsymbol{a} \rangle$ type and edge character for the $\langle \mathbf{a} \rangle$-type dislocations.

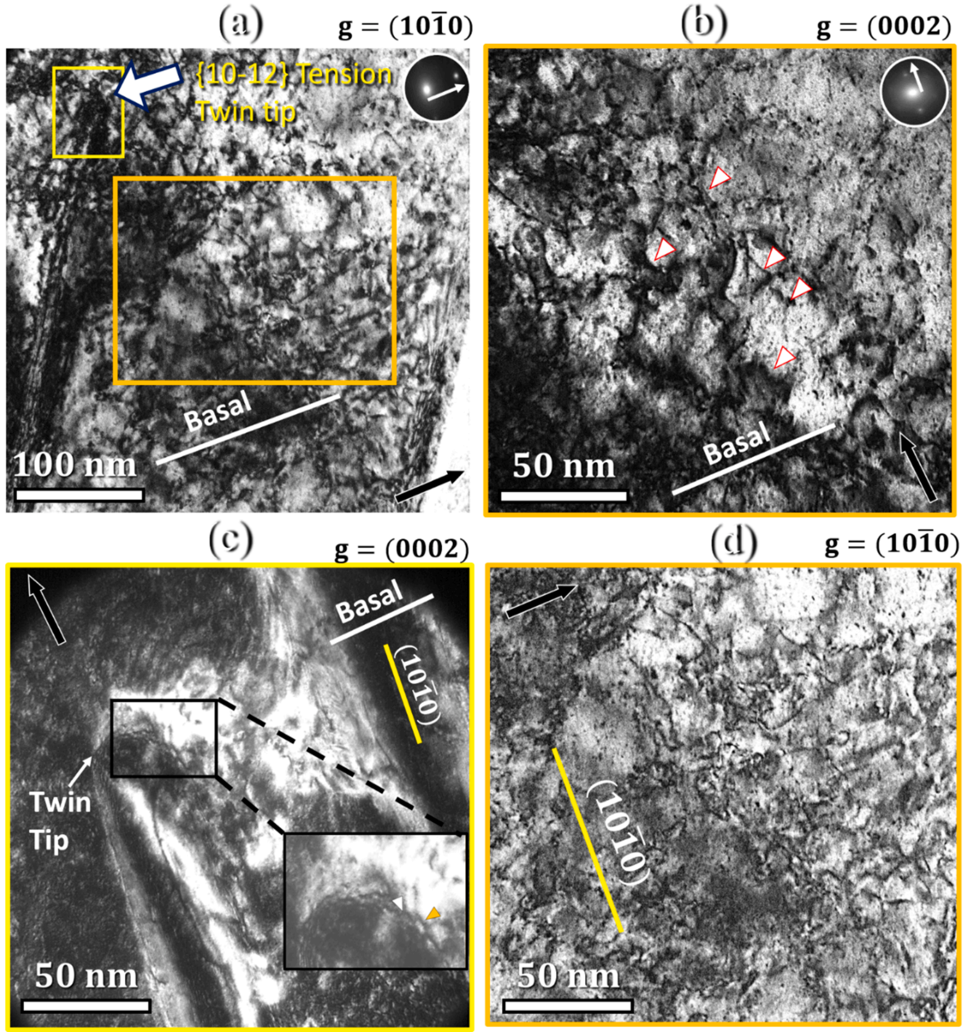

Fig. 11. (a) TEM dislocation analysis at the tip of $\{10\bar{1}2\}$ tension twin and in the neighboring matrix imaged at $g = 10\bar{1}0$. (b) Imaging performed along $g = 0002$ on the matrix highlighted in orange (a), (c) dark-field (DF) TEM imaging performed at $g = 0002$ of the region enclosing the twin tip shown in yellow in (a). (d) Imaging performed along $g = 10\bar{1}0$ of the same region shown in (b). Basal and $(10\bar{1}0)$ traces shown in white and yellow, respectively.

4. Discussion

4.1. Role of local stress vis-à-vis global stress on twinning and slip response

The current work quantifies the local stress gradients arising due to the interaction between a $\{11\bar{2}2\}$ compression twin lamella and a grain boundary. Local stresses were measured both within the grain ahead of the twin-grain boundary interaction zone and within the impinging compression twin. The calculated stress gradients across the interface are fitted to classical dislocation pile-up model described by the Hall-Petch equation (c.f. Fig. 5b), whereby the far field reference stresses (σ_{ref} along *22* direction) are calculated. Subsequently, the difference between the measured residual stress values and the reference stress gives the contribution of twin-grain boundary interaction induced local stresses (as shown in Fig. 5d). Using the analogy of pile up of geometrically necessary dislocations, the stresses generated when a twin hits a grain interface can be associated with the interaction and accommodation of twinning dislocations within the grain boundary. The resultant dislocation accumulation at the twin-grain boundary intersection plane would subsequently result in a forward stress component generated in the neighboring grain, whereas a simultaneous back stress is exerted within the twin, as illustrated in Fig. 12.

In most cubic materials undergoing isotropic plastic deformation (i.e. satisfying the von Mises' criterion [65]), strain compatibility across grain boundary does not play a significant role owing to sufficient geometrically compatible slip systems across the interface that prevent build-up of such back stress and forward stress components due to pile up of dislocations at the interface [13,14,66,67]. However, in anisotropic crystal structures such as hexagonal close packed materials and in particular, with directionally dependent deformation modes such as twinning, evolution of such interfacial stress components cannot be neglected and need to be accurately assessed [66].

Our measured values indicated that while a reference stress state in the neighboring grain i.e., Grain II is described by mean tensile stress of 326 MPa, the twin-boundary interaction generates a local compressive forward stress contribution of −286 MPa in Grain II (c.f. Fig. 5d), due to the dislocation pileup within incident twin. On the other hand, the reference stress state within the compression twin (Twin I) though compressive (given by −28 MPa), experiences a tensile back stress that manifests due to the Twin I-Grain II interface that is measured as 88 MPa.

Here, we provide an analysis of the origins of the forward and back stress components assuming a pile-up of linear array of dislocations at the twin-grain boundary interface (c.f. Fig. 12). The total stress exerted ahead of a pile up of n dislocations in such a case is theoretically

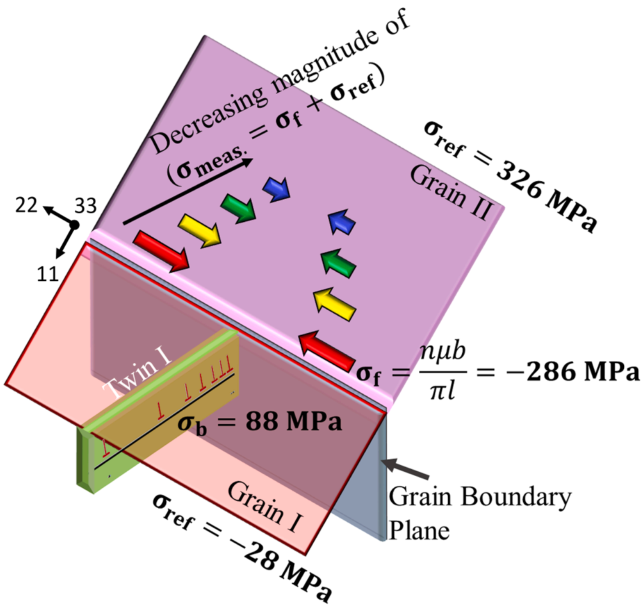

Fig. 12. Schematic illustration of dislocation pile-up inside Twin I at the twin-grain boundary interface. The corresponding stress gradient in Grain II indicated by large compressive stresses at the interface that progressively reduce in magnitude. The direction of arrow indicates the direction of local forward stress component (σ_f) – showing a compressive stress, while the color-coding indicates the relative magnitude of stress with red corresponding to the highest stress magnitude and blue to the lowest. The corresponding tensile back stress value in the twin is given as, $\sigma_b = 88$ *MPa*.

equivalent to the stress generated due to the presence of a single super-dislocation of Burgers vector magnitude: n·|**b**| positioned at the center of gravity of the pile-up in Twin I, given by a distance $\boldsymbol{l}_{\mathbf{pu}}/4$ from the interface [63,68,69]. The resultant stress due to such a super-dislocation would ideally equate to the forward stress σ_f [63,66,70] exerted into Grain II and can be expressed as,

$$\sigma_f = \frac{4n}{l_{pu}} \cdot \frac{\mu_{TwinI} b}{\pi} \tag{5}$$

where, μ_{TwinI} is the shear modulus within Twin I, **b** is the dislocation Burgers vector. It must be noted that here we ignore individual effects of edge and screw components. Also, more importantly we neglect the fact that the complete stress tensorial components should be considered when describing possible slip on anisotropic non-parallel slip systems in Grain II. Just to get a reasonable estimate of the resultant back-stress generated due to the pileup. the same analogy is taken as in the case of the forward stress, i.e.

$$\sigma_b = -\frac{4n}{3l_{pu}} \cdot \frac{\mu_{TwinI} b}{\pi} \tag{6}$$

at a distance of ¾ l_{pu} from a superdislocation nb with a spread-out core and decaying asymptotically to zero at larger distances outside the single pileup. Combining Eqs. (5) and 6, the following relationship within the set of assumptions between the forward and back-stress contributions can be derived, but now taken closer to the interface, where

$$\sigma_f \cong -3 \cdot \sigma_b \tag{7}$$

Interestingly, indeed the experimentally measured forward stress is nearly 3 times larger than the back-stress contribution (c.f. Fig. 5) in the current work i.e., −286 MPa vis-à-vis 88 MPa. This indicates that the experimentally measured local stresses indeed relate to the previously mentioned forward and back stress gradients at twin-grain boundary interface. The high dislocation density observed near the interface, within Twin I, in Fig. 10a and 10b is thus attributed to the dislocation pileup within the impinging twin.

The magnitude of σ_f can be further quantified on the basis of the experimentally measured dislocation density values shown in Fig. 5a. For large dislocation density values, the parameter $\frac{n}{(l_{pu/4})}$ in Eq. (5) can be approximated as the square root of GND density measured at the twin-grain boundary interface: $\sqrt{\rho_{GND}}$. Substituting the measured $\boldsymbol{\rho}_{\mathbf{GND}}$ for $\langle a \rangle$-type dislocations (from Fig. 5a) in Eq. (5) we obtain 314 MPa. The good agreement between estimates based upon GND density and the experimentally measured magnitude of σ_f (c.f. Fig. 5d), reinforces the fact that the measured stress fields arise due to the interaction between dislocations within the twin and the geometrically necessary dislocations (GND) at the twin-grain boundary interface. The model used in the paper describes the stress gradient as a pile up of GNDs. It is agreed that physically the pile-up in the twin leads to forward stress exerted at the tip of the pile-up into the neighboring grain and a back stress due to the pile-up on the twin. The magnitudes of the forward stresses are correlated to a virtual dislocation pile-up in the neighboring grain to show that the measured GND density at the interface points to such a forward stress value. As a matter of course the HP-analysis does not describe the rather complex structure of the debris of dislocations which surround the twins, see e.g. in Fig. 10. Here HP provides a toolbox for stress analysis rather than a diorama upon 3D dislocation configurations.

One of the central themes of the current study is to quantify the role of local vs. global stress states on the local plastic deformation. In the following, we assess if the local stress values quantified above are significant enough to trigger plasticity, near the twin-grain boundary interface. Considering the yield strength of about 200 MPa (see above 2.1 and [71]), the corresponding critical resolved shear stress (would be of the order of 70–100 MPa ($\frac{\sigma_y}{3}$ (Taylor) $\leq \tau_{CRSS} \leq \frac{\sigma_y}{2}$ (Sachs)). Such low threshold shear stress values suggests that the twin-grain boundary interaction stresses measured in the present work ($\boldsymbol{\sigma}_{\mathbf{f}}$ as −286 MPa) are high enough to induce local scale plasticity within Grain II.

The aforementioned hypothesis is further validated by the deformation microstructure observed in the region near the twin-grain boundary interaction zone (see Fig. 7), as will be elucidated in the current paragraph. Fig. 13a and 13b present the maximum Schmid Factor (SF) maps (i.e., for the twin variant with the highest SF) for the twin-grain boundary interaction region calculated for $\{11\overline{2}2\}$ and $\{10\overline{1}2\}$ twinning modes corresponding to tensile loading (globally applied stress) and compressive loading (local forward stress), respectively. The maps in Fig. 13a indicate that under applied tension, there is a strong preference of $\{11\overline{2}2\}$ compression twinning over $\{10\overline{1}2\}$ tension twinning in Grain II. Note that the tensile stress in Fig. 13a is resolved along the *22* direction, such that $\sigma_{22} = \sigma_{TD} \cdot \cos 12^\circ$, giving σ_{22} as $0.84\sigma_{TD}$. On the other hand, the SF maps indicate a higher SF for $\{10\overline{1}2\}$ tension twinning over $\{11\overline{2}2\}$ compression twinning when considering compressive stresses acting along *22* (c.f. Fig. 13b). The SF values within Grain II associated with globally applied tension contradict the observed twinning response in Figs. 7 and 8. Rather, the appearance of profuse tension twinning in Grain II shows greater conformity with the SF values based on the local forward stress contribution stemming from the twin-grain boundary interaction (shown in Fig. 13b). Fig. 13a also shows that the twin transmission parameter for compression twinning across Grain I/Grain II interface gives a value of $m' = 0.65$, geometrically indicating easy twin transfer across the grain boundary. However, the microstructure of the region at the vicinity of the twin-grain boundary interface (shown in Fig. 7) indicates negligible fraction of compression twins vis-à-vis a high fraction of tension twinning within Grain II, thus depicting a local deformation microstructure that is counterintuitive to the strain accommodation mechanisms predicted by the geometric compatibility of twin transmission across the grain boundary. Correlating the SF maps (Fig. 13) and the deformation microstructure in Figs. 7 and 8, it is proposed that the local forward stress component dictates the resultant local mechanical response at the

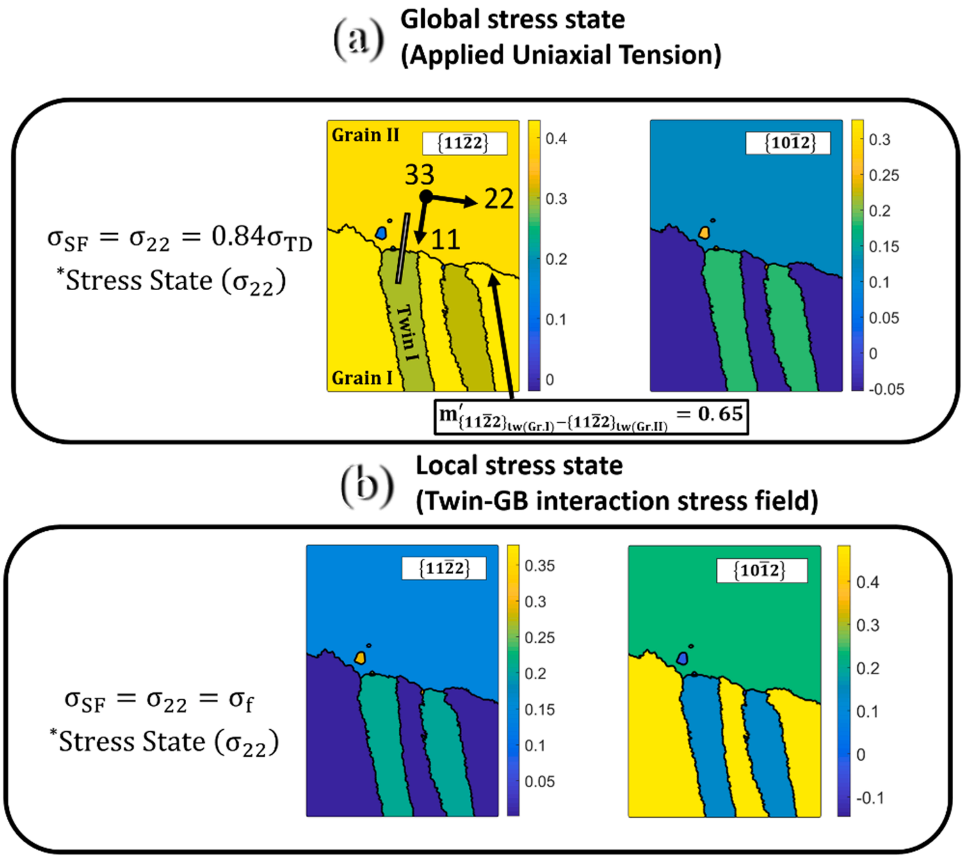

Fig. 13. (a) Maximum Schmid factor maps (Twin variant with the largest Schmid factor) corresponding to $\{11\bar{2}2\}$ compression twinning and $\{10\bar{1}2\}$ tension twinning considering tensile loading along σ_{22}. The geometrical twin transmission parameter m' across Grain I/Grain II for $\{11\bar{2}2\}$ compression twin is calculated as 0.65. (b) Maximum Schmid factor maps (Twin with the largest Schmid factor) corresponding to $\{11\bar{2}2\}$ compression twinning and $\{10\bar{1}2\}$ tension twinning considering compressive loading along σ_{22}.

vicinity of the grain boundary rather than the globally applied tensile stress.

Our findings also highlight the stark deviations between twin transmission predictions based upon geometrical compatibility vis-à-vis realistic deformation microstructures. This indicates that local twin-grain boundary interaction induced stresses are critical when considering strain compatibility across interfaces and sole assessment based upon geometric measure results in low fidelity in terms of predicting local plasticity behavior. It is interesting to note that the macroscale deformation response in Grain II corresponds nicely with the SF maps under global tensile loading (see Fig. 13a) as indicated by the presence of large $\{11\bar{2}2\}$ compression twins traversing the whole grain (as shown in Fig. 4), thus emphasizing the contrasting behavior when comparing macro- and micro-scale plasticity response.

Tension twinning in Grain II gave rise to formation of multiple twin variants. Theoretically, tension twinning can occur on six crystallographically equivalent $\{10\bar{1}2\}$ habit planes giving rise to six possible variants [36]. Realistically, however, tension twinning in Mg and Ti is typically highlighted by strong variant selection, wherein the dominant twin variant corresponds to the one with the largest Schmid Factor [37,72,73]. In the present study, the tension twins observed in the Grain II indicate a *non-Schmid* type twin variant selection, with three different twin variants nucleating ahead of the twin-grain boundary interaction zone. Fig. 14a shows the simulated single orientation scatter data highlighting the twin orientations observed in grain II. The corresponding Schmid factor values are outlined in Fig. 14b. Two stress states are considered, viz. for applied tensile stress along *22* and compressive local stress along *22*. The former stress state gives rise to zero or negative Schmid factor values (i.e., the associated twinning strain is opposite to the imposed deformation), thus indicating that the nucleation of the experimentally observed twin variants in Figs. 7 and 8, considering the global tensile stress is not feasible. On the other hand, the positive

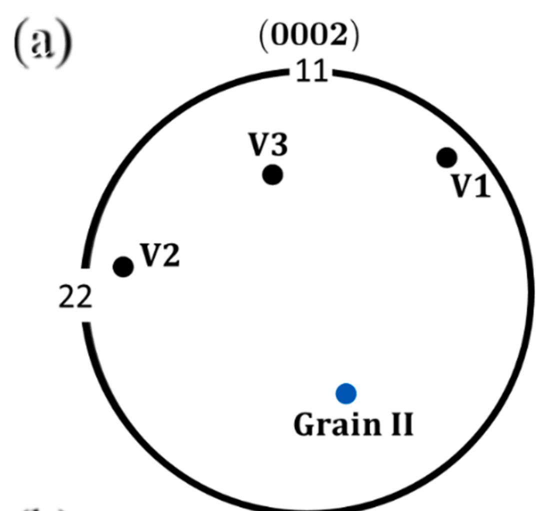

(b)

Calculated Schmid Factor values for experimentally observed $\{10\bar{1}2\}$ twin variants

Stress State	V1	V2	V3
Local compressive forward stress	0.14	0.23	0.33
Applied Tensile stress	0.08	-0.24	-0.45

Fig. 14. (a) Simulated single orientation scatter plot showing the experimentally observed twin variants in Grain II. The shown variants viz. V1, V2 and V3 correspond to the three highest Schmid factor values out of the 6 possible variants (considering compressive stress along σ_{22}); (b) Calculated Schmid factors for V1, V2 and V3 considering compressive (local forward stress) and tensile loading (globally applied stress) along σ_{22}.

Schmid factor values for tensile twinning assuming a compressive stress along *22* indicates that the observed twinning response is attributed to the local compressive forward stress generated by the twin-grain boundary interaction. The lack of variant selection most likely arises from the complex local stress states that not only see contributions from twin-grain boundary interaction stresses but also due to twinning induced accommodation stresses within the grain (that will be discussed in the next paragraph), whereby twin variants that violate the Schmid rule are also able to nucleate. Along similar lines, appearance of $\{11\overline{2}2\}$, $\{11\overline{2}4\}$ and $\{10\overline{1}1\}$ compression twins within Twin I close to the twin-grain boundary intersection zone is attributed to a tensile back stress component that would ideally act normal to the c-axis of the green $\{11\overline{2}2\}$ twin (in Fig. 7) thus favoring compression twins.

Twin formation within a grain is associated with large strain fields that give rise to in-grain stresses in addition to the aforementioned twin-grain boundary interaction stresses. The net local stresses are hence a superposition of these stress fields. The stress fields arising from twin formation correspond to coherency strains that arise due to twin accommodation effects [25,74–76]. The large dislocation density near twins, as observed in Figs. 10 and 11, alludes to such accommodation strains associated with twin formation. Fig. 15a shows presence of large strain fields around a tension twin that forms inside grain II. The ripple contour seen in the DF-TEM diffraction contrast indicates the local lattice distortion at the vicinity of the twin, with brighter regions corresponding to areas with larger accumulated strain and dislocation pile-up. This is corroborated by the inset GROD map in Fig. 15a, where the Grain Reference Orientation Deviation (GROD) angle provides the misorientation angle with respect to a reference orientation of a grain on a local level. The width of the strain field is nearly 10 times the maximum twin width, thereby indicating that the range of influence of these elastic stresses can be significant. The maximum strain is observed at the twin tips and is associated with a pile-up of non-basal dislocations as seen in Fig. 11c. Theoretically the linear-elastic energy generated by a non-basal dislocation is approx. 7 times the linear-elastic energy of basal dislocation, since the,

$$\frac{E_{non-basal}}{E_{basal}} \propto \frac{\boldsymbol{b}_{c+a}\cdot\boldsymbol{b}_{c+a}}{\boldsymbol{b}_a\cdot\boldsymbol{b}_a} \tag{8}$$

thus, indicating that the presence of $\langle \boldsymbol{c} + \boldsymbol{a} \rangle$ dislocations can act as primary stress contributors at the twin tip. An estimate of the stress fields ahead of the tension twin tip is presented by the experimentally determined dislocation density gradients that decay as a function of square root of distance from the twin tip, shown in Fig. 15b. Considering that the $\langle \boldsymbol{c} + \boldsymbol{a} \rangle$-type GND density at the twin tip is of the order of $10^{16}\ m^{-2}$ (c.f. Fig. 15b), the corresponding local stress magnitude can be given as:

$$\sigma_{\text{twin-tip}} = \frac{\mu b_{\langle c+a \rangle}}{\pi l} = \sqrt{\rho_{\text{GND}\langle c+a \rangle}}\frac{\mu b_{\langle c+a \rangle}}{\pi} \tag{9}$$

which generates a substantially high local stress concentration of ~800 MPa. Depending upon the nature of stress i.e., tensile or compressive, such large magnitudes of stress fields present at twin tips can locally trigger instabilities such as crack formation (Fig. 6) or be relieved through local plasticity via. slip and twinning events (Figs. 7, 9 and 11).

Fitting of the measured stress gradients in Twin I and Grain II to a Hall-Petch type dependence gives the corresponding obstacle strength factors of 0.093 MPa.$m^{-1/2}$ and 0.198 MPa.$m^{-1/2}$, respectively (Fig. 5b). These values are rather low when compared to the grain boundary strength reported for polycrystalline Ti, which is ~ 0.4 MPa.$m^{-1/2}$ [62]. It is proposed that the accommodation of the twin within the grain boundary locally weakens the obstacle strength. It is likely that the impinging twin locally induces a change in the grain boundary structure, whereby the accommodation of twin at the interface results in a non-equilibrium configuration of grain boundary dislocations. When the grain boundary dislocation cores become more localized by the twin interaction, the necessary nucleation shear stress at the grain boundary is decreased leading to lowering of the Hall-Petch obstacle strength, k_{HP}. In addition, through the twin-GB interactions ledges are formed which can act as a source of dislocations in Grain II. The size of the ledge depends upon the number of twin dislocations causing heterogeneous shear of the boundary plane and/or the number of resulting grain-boundary dislocations within the twin-GB interface to form a ledge [77].

The observation of shear coupled grain boundary migration induced by the twin-grain boundary interaction (as seen in Fig. 4e) suggests the role of the interface locally acting as a dislocation nucleation source rather than contributing to dislocation strengthening.

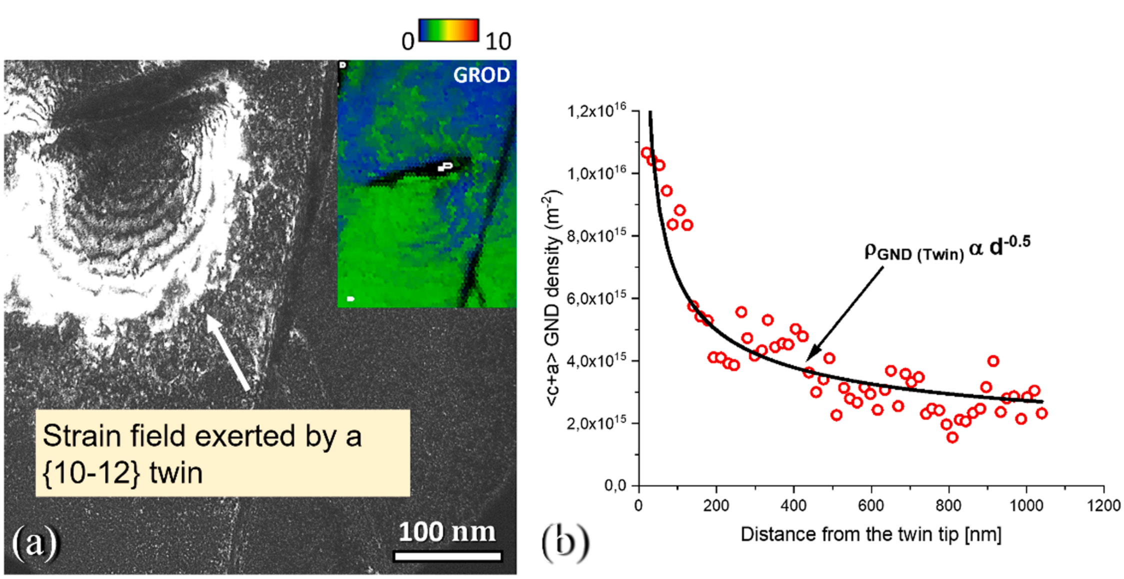

Fig. 15. (a) DF-TEM imaging showing the diffraction contrast due to the strain field exerted by a $\{10\overline{1}2\}$ tension twin, inset image indicates the angular grain reference orientation deviation (GROD) map of the same region, indicating large lattice rotations at the vicinity of the twin. (b) The GND density gradient ahead of the twin tip, with maximum values of the order of $10^{16}m^{-2}$ near the tip that decay as a function of one over square root of distance on moving away from the tip.

4.2. Role of twin interfacial structures on local stress fields for different twinning modes

In order to evaluate the nature and magnitude of stress fields generated by twins, it is imperative to characterize the twin interfacial structure. It is well known that the depending on nature of twin type in hexagonal close packed metals, their energetically feasibility to nucleate and grow can be starkly contrasting [36]. For instance, it is well known that $\{10\bar{1}2\}$ tension twins are invariably prone to nucleate and migrate at very low shear stresses, thereby enabling easy c-axis strain accommodation in the absence of non-basal slip modes [25]. The underlying mechanism, as mentioned previously is attributed to atomic shuffling dominated twin boundary motion with negligible dislocation shearing. On the other hand, compression twins such as $\{10\bar{1}1\}$ and $\{11\bar{2}2\}$ types, that undergo slip mediated migration require much higher stresses to propagate such that they often lead to localized stress concentrations at the twin-matrix interface, which in the absence of suitable non-basal dislocation slip can potentially lead to crack nucleation.

Interestingly, on comparing the twin boundary energies of $\{10\bar{1}2\}$ and $\{11\bar{2}2\}$ twins in **α**-Ti, the values are rather similar i.e. 304 mJ.m^{-2} [78] vis-à-vis 285 mJ.m^{-2} [79] respectively. These values indicate that the observed difference in twin growth mechanisms and the corresponding impact on the local stresses for different twinning modes cannot be explained on the basis of coherent twin boundary energies. Furthermore, considering that the twinning shears associated with $\{10\bar{1}2\}$ tension twins and compression twins are comparable i.e. $\gamma_{\{10\bar{1}2\}} = 0.18$ and $\gamma_{\{11\bar{2}2\}} = 0.22$ [26], the high mobility of the former twin type and the sluggish growth of latter [80] is rather contrasting from the perspective of twin formation and migration energies. Here, it is argued that the underlying difference most likely stems from the different twin interface geometry that corresponds to different twin types.

Twin interfaces though ideally known to be coherent symmetric-tilt boundaries show a strong tendency of faceting along the twin boundary, wherein the facets can be of non-tilt or mixed character depending on the twin type [81]. The appearance of facets purely arises considering the 3-dimensional shape of twin lamella, wherein geometric compatibility effects lead to interfacial pile-up of dislocations that are subsequently relaxed by creation of boundary segments existing as non-invariant interfaces with a different crystallographic orientation than that of the coherent twin boundary [81,82]. One of the most commonly observed $\{10\bar{1}2\}$ tension twins in hexagonal materials is associated with Basal-Prismatic/Prismatic-Basal (BP/PB) facets as shown in Fig. 16b. It has been shown in earlier works that the BP/PB facets in tension twins form during the process of twin nucleation and migration that involves dislocation transmutation, wherein dislocations from the matrix are partially absorbed and partly transmitted across the twin-matrix interface [6,80,83,84]. The transmutation process consequently induces twin boundary shearing resulting in appearance of BP/PB facets and additionally result in mobile $\frac{1}{17}\langle 10\bar{1}1\rangle$ twinning

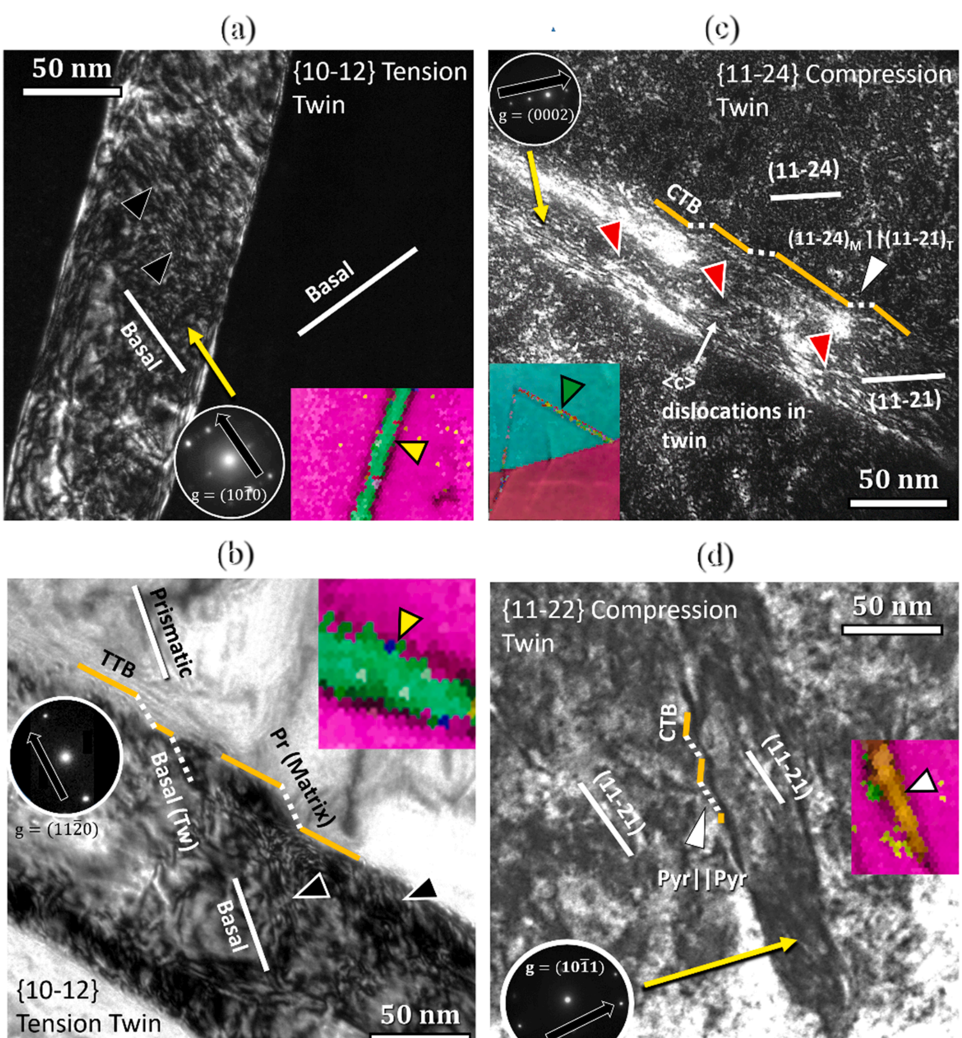

Fig. 16. (a) Structure of $\{10\bar{1}2\}$ tension twin, indicating high density of basal stacking faults within the twin, (b) appearance of Basal-Prismatic facets along the $\{10\bar{1}2\}$ twin boundary, black arrowheads with white outline indicate basal I2 stacking faults. (c) Twin boundary facets observed in $\{11\bar{2}4\}$ compression twins that are crystallographically described by $\{11\bar{2}4\}_{matrix}||\{11\bar{2}1\}_{twin}$; red arrow heads with white outline indicate ⟨c⟩ dislocations within the twin. (d) Twin boundary facets observed in $\{11\bar{2}2\}$ compression twins that are crystallographically described by $\{11\bar{2}1\}_{matrix}||\{11\bar{2}1\}_{twin}$ (Pyr-Pyr facets). Coherent Twin Boundary (CTB) segments are shown in orange guiding lines and the twin facets are indicated by white dotted lines. Inset images in each show the EBSD IPF map of the imaged twin. Yellow arrowheads with black outline indicate $\{10\bar{1}2\}$ tension twins, white arrowheads with black outline indicate $\{11\bar{2}2\}$ compression twins and green arrowheads with black outline show the $\{11\bar{2}4\}$ compression twins.

dislocations that glide along the coherent twin boundary segments [6, 80]. The glide of each twinning dislocation along the twin interface propels the migration of the twin boundary by one unit step. Simultaneously, the residual misfit dislocations generated at the BP facet can move along with the twin boundary, leaving behind I_2 basal stacking faults as indicated by the high density of stacking faults within the twin [83] observed in Fig. 16a and 16b. Fig. 16c and 16d indicate that the facets formed along the $\{11\overline{2}4\}$ and $\{11\overline{2}2\}$ compression twins (it must be noted that both twins form a conjugate pair i.e. same axis and shear, hence energetically and topologically should behave similarly) correspond to Pyramidal-Pyramidal (Py-Py) planes matching across the twin and the matrix.

In the case of $\{11\overline{2}4\}$ twin, the observed facet is described by $\{11\overline{2}4\}\|\{11\overline{2}1\}$ plane (Fig. 16c). On the other hand, the $\{11\overline{2}2\}$ twin gives rise to $\{11\overline{2}1\}\|\{11\overline{2}1\}$ facets (Fig. 16d). Our observations for $\{11\overline{2}2\}$ twin agree with the facet observations earlier reported in Refs. [79] and [85]. Ref. [79] performed a 3-dimensional structural characterization, reporting the presence of $\{11\overline{2}1\}\|\{11\overline{2}1\}$ and six other crystallographically distinct facets that are associated with $\{11\overline{2}2\}$ twins.

The formation of such facets along the twin-matrix interface is associated with coherency strains giving rise to the observed stress fields at the vicinity of the twins (c.f. Fig. 15). Intuitively at the twin tips, where the twin boundary loses most of its coherency the density of such facets will be the maximum and subsequently the local strain fields will be concentrated in these regions. This explains the high density of $\langle \boldsymbol{c} + \boldsymbol{a} \rangle$ dislocations piling up within the matrix ahead of the twin tips (c.f. Fig. 11a and 11c) and the previously estimated large stresses in this zone. The magnitude of strain generated would thus directly correspond to dislocation energy resulting from the accumulation of misfit dislocations at the twin facets. An estimate of elastic energy associated with different facet types gives significantly large values for Py-Py facets observed in $\{11\overline{2}2\}$ twins (c.f. Fig. 16c and 16d), of the order of 450 mJ.m^{-2} [79] compared to BP/PB facets (c.f. Fig. 16b) that correspond to values between 97 - 174 mJ.m^{-2} [86–88]. The presence of $\langle \boldsymbol{c} \rangle$ dislocations within the $\{11\overline{2}2\}$ twin (shown in Fig. 16c) validates the higher elastic energy of the facets that require the participation of difficult to activate non-basal dislocation slip (higher migration stresses) in order to accommodate the local strain across the twin interface.

On the other hand, lower elastic energies for the BP/PB facets indicate their relative ease of migration, thus requiring lower applied stress. The elastic energy estimates thus explain the marked reduction in mobility of compression twins vis-à-vis tension twins and the subsequent impact of the former twin boundary type in triggering failure due to build-up of local stresses, in the absence of sufficient non-basal deformation modes. This is indicated in the current work by the grain boundary shearing induced by the impinging $\{11\overline{2}2\}$ compression twin as well as the appearance of fracture sites along the grain boundary, indicative of an inhomogeneous strain accommodation response at the grain boundary.

5. Conclusions

The present work outlines the impact of local stress gradients vis-à-vis global stress on microscale plasticity and failure mechanisms in twinned microstructures in hcp materials. Stress gradients ahead of a $\{11\overline{2}2\}$ compression twin-grain boundary interaction and corresponding back stresses within the impinging twin are quantified. Correlative nanoscale structural characterization at the vicinity of the twin-grain boundary interaction zone is utilized to unravel the role of local stress gradients on the deformation structure. The following key conclusions are derived:

(1) Compressive stress gradients are quantified ahead of the twin-grain boundary interaction I α-Ti, with the peak forward stress at the tip of the intersection measured as −286 MPa. The corresponding back-stress gradient within the twin is of a tensile nature, peaking at 88 MPa at the interface.
(2) Stresses arising from the twin-grain boundary interaction dictate the microscale twinning response at the vicinity of the interface, rather than the globally applied tensile stress. On the other hand, the macroscale deformation within the bulk grain correlates well to the globally applied stress as shown by formation of large $\{11\overline{2}2\}$ compression twins.
(3) The twin-grain boundary interaction strain mediated local plasticity contradicts the strain accommodation modes predicted on the basis of geometrical compatibility of deformation modes and global Schmid factor values.
(4) Twin-grain boundary interaction locally weakens the obstacle strength of the grain boundary, whereby the local grain boundary structure exhibits a non-equilibrium dislocation configuration that acts as a dislocation source rather than a sink.
(5) Twin boundary facets are experimentally determined for $\{11\overline{2}4\}$ and $\{11\overline{2}2\}$ compression twins, wherein the former is associated with $\{11\overline{2}4\}\|\{11\overline{2}1\}$ and the latter comprises $\{11\overline{2}1\}\|\{11\overline{2}1\}$ facets. $\{10\overline{1}2\}$ tension twins generate the already established basal-prismatic/prismatic-basal facets.
(6) It is shown that the low threshold stress for growth of tension twins in contrast to significantly larger nucleation and propagation stress of compression twins is attributed to the crystallography of twin boundary facet and associated elastic energy. The facet energy also explains the experimentally observed sluggish migration rates of compression twins and their role in promoting localized failure.

Declaration of Competing Interest

The authors declare that they have no known competing financial interests or personal relationships that could have appeared to influence the work reported in this paper

Acknowledgements

The authors thank the Scientific Center for Optical and Electron Microscopy (ScopeM), ETH Zurich, for access to its electron microscopy facilities.

References

[1] H. Wu, G. Fan, An overview of tailoring strain delocalization for strength-ductility synergy, Prog. Mater Sci. 113 (2020), 100675.
[2] E. Ma, T. Zhu, Towards strength–ductility synergy through the design of heterogeneous nanostructures in metals, Mater. Today 20 (6) (2017) 323–331.
[3] I. Basu, M. Chen, J. Wheeler, R.E. Schäublin, J.F. Löffler, Stacking-fault mediated plasticity and strengthening in lean, rare-earth free magnesium alloys, Acta Mater. (2021), 116877.
[4] I. Basu, J.T.M. De Hosson, Strengthening mechanisms in high entropy alloys: fundamental issues, Scr. Mater. 187 (2020) 148–156.
[5] Y. Wang, M. Chen, F. Zhou, E. Ma, High tensile ductility in a nanostructured metal, Nature 419 (6910) (2002) 912–915.
[6] I. Basu, M. Chen, J. Wheeler, R.E. Schäublin, J.F. Löffler, Segregation-driven exceptional twin-boundary strengthening in lean Mg–Zn–Ca alloys, Acta Mater. 229 (2022), 117746.
[7] E. Ma, X. Wu, Tailoring heterogeneities in high-entropy alloys to promote strength–ductility synergy, Nat. Commun. 10 (1) (2019) 5623.
[8] I. Basu, V. Ocelík, J.T.M. De Hosson, Size dependent plasticity and damage response in multiphase body centered cubic high entropy alloys, Acta Mater. 150 (2018) 104–116.
[9] I. Basu, T. Al-Samman, Hierarchical twinning induced texture weakening in lean magnesium alloys, Front. Mater. 6 (2019).
[10] Y. Liu, J. Sun, Y. Fu, B. Xu, B. Li, S. Xu, P. Huang, J. Cheng, Y. Han, J. Han, G. Wu, Tuning strength-ductility combination on selective laser melted 316L stainless steel through gradient heterogeneous structure, Addit. Manuf. 48 (2021), 102373.

[11] H. Fu, B. Ge, Y. Xin, R. Wu, C. Fernandez, J. Huang, Q. Peng, Achieving high strength and ductility in magnesium alloys via densely hierarchical double contraction nanotwins, Nano Lett. 17 (10) (2017) 6117–6124.
[12] X.F. Xie, Z.M. Xie, R. Liu, Q.F. Fang, C.S. Liu, W.Z. Han, X. Wu, Hierarchical microstructures enabled excellent low-temperature strength-ductility synergy in bulk pure tungsten, Acta Mater. 228 (2022), 117765.
[13] X. Wu, Y. Zhu, Heterogeneous materials: a new class of materials with unprecedented mechanical properties, Mater. Res. Lett. 5 (8) (2017) 527–532.
[14] Y. Zhu, X. Wu, Heterostructured materials, Prog. Mater Sci. 131 (2023), 101019.
[15] I. Basu, V. Ocelík, J.T.M. De Hosson, Measurement of spatial stress gradients near grain boundaries, Scr. Mater. 136 (2017) 11–14.
[16] R. Maaß, P.M. Derlet, Micro-plasticity and recent insights from intermittent and small-scale plasticity, Acta Mater. 143 (2018) 338–363.
[17] X. Zhang, J. Xiong, H. Fan, M. Zaiser, Microplasticity and yielding in crystals with heterogeneous dislocation distribution, Modelling and Simulation in, Mater. Sci. Eng. 27 (7) (2019), 074003.
[18] Y. Guo, H. Abdolvand, T.B. Britton, A.J. Wilkinson, Growth of $\{11\bar{2}2\}$ twins in titanium: a combined experimental and modelling investigation of the local state of deformation, Acta Mater. 126 (2017) 221–235.
[19] Y. Guo, T.B. Britton, A.J. Wilkinson, Slip band–grain boundary interactions in commercial-purity titanium, Acta Mater. 76 (2014) 1–12.
[20] Y.J. Chen, Y.J. Li, J.C. Walmsley, N. Gao, H.J. Roven, M.J. Starink, T.G. Langdon, Microstructural heterogeneity in hexagonal close-packed pure Ti processed by high-pressure torsion, J. Mater. Sci. 47 (12) (2012) 4838–4844.
[21] S. Zhao, R. Zhang, Q. Yu, J. Ell, R.O. Ritchie, A.M. Minor, Cryoforged nanotwinned titanium with ultrahigh strength and ductility, Science 373 (6561) (2021) 1363–1368.
[22] M.A. Kumar, I.J. Beyerlein, Local microstructure and micromechanical stress evolution during deformation twinning in hexagonal polycrystals, J. Mater. Res. 35 (3) (2020) 217–241.
[23] M.H. Yoo, J.K. Lee, Deformation twinning in h.c.p. metals and alloys, Philos. Mag. A 63 (5) (1991) 987–1000.
[24] M.H. Yoo, S.R. Agnew, J.R. Morris, K.M. Ho, Non-basal slip systems in HCP metals and alloys: source mechanisms, Mater. Sci. Eng. A 319-321 (2001) 87–92.
[25] M.H. Yoo, Slip, twinning, and fracture in hexagonal close-packed metals, Metall. Trans. A 12 (3) (1981) 409–418.
[26] P.G. Partridge, The crystallography and deformation modes of hexagonal close-packed metals, Metall. Rev. 12 (1) (1967) 169–194.
[27] J. Hirsch, T. Al-Samman, Superior light metals by texture engineering: optimized aluminum and magnesium alloys for automotive applications, Acta Mater. 61 (3) (2013) 818–843.
[28] I. Basu, H. Fidder, V. Ocelík, J. Th, Local stress states and microstructural damage response associated with deformation twins in hexagonal close packed metals, Crystals 8 (1) (2018) 1.
[29] Z. Shen, R.H. Wagoner, W.A.T. Clark, Dislocation and grain boundary interactions in metals, Acta Metall. 36 (12) (1988) 3231–3242.
[30] W.A.T. Clark, R.H. Wagoner, Z.Y. Shen, T.C. Lee, I.M. Robertson, H.K. Birnbaum, On the criteria for slip transmission across interfaces in polycrystals, Scr. Metall. Mater. 26 (2) (1992) 203–206.
[31] T.C. Lee, I.M. Robertson, H.K. Birnbaum, Prediction of slip transfer mechanisms across grain boundaries, Scr. Metall. 23 (5) (1989) 799–803.
[32] M. Arul Kumar, I.J. Beyerlein, R.J. McCabe, C.N. Tomé, Grain neighbour effects on twin transmission in hexagonal close-packed materials, Nat. Commun. 7 (1) (2016) 13826.
[33] M.R. Barnett, M.D. Nave, A. Ghaderi, Yield point elongation due to twinning in a magnesium alloy, Acta Mater. 60 (4) (2012) 1433–1443.
[34] N.S. Prasad, N. Naveen Kumar, R. Narasimhan, S. Suwas, Fracture behavior of magnesium alloys – Role of tensile twinning, Acta Mater. 94 (2015) 281–293.
[35] D. Ando, J. Koike, Y. Sutou, The role of deformation twinning in the fracture behavior and mechanism of basal textured magnesium alloys, Mater. Sci. Eng. A 600 (2014) 145–152.
[36] I. Basu, T. Al-Samman, Twin recrystallization mechanisms in magnesium-rare earth alloys, Acta Mater. 96 (2015) 111–132.
[37] J.J. Jonas, S. Mu, T. Al-Samman, G. Gottstein, L. Jiang, Ė. Martin, The role of strain accommodation during the variant selection of primary twins in magnesium, Acta Mater. 59 (5) (2011) 2046–2056.
[38] S. Mu, J.J. Jonas, G. Gottstein, Variant selection of primary, secondary and tertiary twins in a deformed Mg alloy, Acta Mater. 60 (5) (2012) 2043–2053.
[39] J. Wang, M.R.G. Ferdowsi, P.A. Lynch, S.R. Kada, M.R. Barnett, Influence of precipitation on tension and compression twinning in Mg-6.5Zn alloy, Scr. Mater. 207 (2022), 114253.
[40] M.R. Barnett, Twinning and the ductility of magnesium alloys: part I: "Tension" twins, Mater. Sci. Eng. A 464 (1) (2007) 1–7.
[41] M.R. Barnett, Twinning and the ductility of magnesium alloys: part II. "Contraction" twins, Mater. Sci. Eng. A 464 (1) (2007) 8–16.
[42] B. Li, X.Y. Zhang, Global strain generated by shuffling-dominated $\{10\bar{1}2\}\langle 10\bar{1}\bar{1}\rangle$twinning, Scr. Mater. 71 (2014) 45–48.
[43] Q. Zu, X.Z. Tang, S. Xu, Y.F. Guo, Atomistic study of nucleation and migration of the basal/prismatic interfaces in Mg single crystals, Acta Mater. 130 (2017) 310–318.
[44] J. Jeong, M. Alfreider, R. Konetschnik, D. Kiener, S.H. Oh, In-situ TEM observation of $\{10\bar{1}2\}$ twin-dominated deformation of Mg pillars: twinning mechanism, size effects and rate dependency, Acta Mater. 158 (2018) 407–421.
[45] J. Li, M. Sui, B. Li, A half-shear-half-shuffle mechanism and the single-layer twinning dislocation for $\{11\bar{2}2\}\langle 11\bar{2}\bar{3}\rangle$ mode in hexagonal close-packed titanium, Acta Mater. 216 (2021), 117150.
[46] Q. Zu, X.Z. Tang, H. Fu, Q.M. Peng, Y.F. Guo, The irrational shear of $\{10\bar{1}1\}$ twinning in Mg, Materialia 5 (2019), 100239.
[47] A. Ostapovets, R. Verma, A. Serra, Unravelling the nucleation and growth of $\{11\bar{2}2\}$ twins, Scr. Mater. 215 (2022), 114730.
[48] M. Yuasa, M. Hayashi, M. Mabuchi, Y. Chino, Atomic simulations of, twinning and detwinning in magnesium, J. Phys. Condens. Matter 26 (1) (2014), 015003.
[49] G. Gottstein, Physical Foundations of Materials Science, Springer Science & Business Media, 2013.
[50] F. Bachmann, R. Hielscher, H. Schaeben, Texture analysis with MTEX – free and open source software toolbox, Solid State Phenomena 160 (2010) 63–68.
[51] K.J. Kang, N. Yao, M.Y. He, A.G. Evans, A method for in situ measurement of the residual stress in thin films by using the focused ion beam, Thin Solid Films 443 (1) (2003) 71–77.
[52] C. Mansilla, D. Martínez-Martínez, V. Ocelík, J.T.M. De Hosson, On the determination of local residual stress gradients by the slit milling method, J. Mater. Sci. 50 (10) (2015) 3646–3655.
[53] C. Mansilla, V. Ocelík, J.T.M. De Hosson, A new methodology to analyze instabilities in SEM imaging, Microsc. Microanal. 20 (6) (2014) 1625–1637.
[54] T.B. Britton, H. Liang, F.P.E. Dunne, A.J. Wilkinson, The effect of crystal orientation on the indentation response of commercially pure titanium: experiments and simulations, Proc. R. Soc. A Math. Phys. Eng. Sci. 466 (2115) (2010) 695–719.
[55] R. van Bremen, D. Ribas Gomes, L.T.H. de Jeer, V. Ocelík, J.T.M. De Hosson, On the optimum resolution of transmission-electron backscattered diffraction (t-EBSD), Ultramicroscopy 160 (2016) 256–264.
[56] S.I. Wright, M.M. Nowell, S.P. Lindeman, P.P. Camus, M. De Graef, M.A. Jackson, Introduction and comparison of new EBSD post-processing methodologies, Ultramicroscopy 159 (2015) 81–94.
[57] T. Vystavěl, L. Tůma, P. Stejskal, M. Unčovský, J. Skalický, R. Young, Expanding capabilities of low-kV STEM imaging and transmission electron diffraction in FIB/SEM systems, Microsc. Microanal. 23 (S1) (2017) 554–555.
[58] M.F. Ashby, The deformation of plastically non-homogeneous materials, Philos. Mag. A J. Theor. Exp. Appl. Phys. 21 (170) (1970) 399–424.
[59] P.J. Konijnenberg, S. Zaefferer, D. Raabe, Assessment of geometrically necessary dislocation levels derived by 3D EBSD, Acta Mater. 99 (2015) 402–414.
[60] E.O. Hall, The deformation and ageing of mild steel: III discussion of results, Proc. Phys. Soc. London Sect. B 64 (9) (1951) 747.
[61] A. Cracknell, N.J. Petch, Frictional forces on dislocation arrays at the lower yield point in iron, Acta Metall. 3 (2) (1955) 186–189.
[62] R. Armstrong, I. Codd, R.M. Douthwaite, N.J. Petch, The plastic deformation of polycrystalline aggregates, Philos. Mag. A J. Theor. Exp. Appl. Phys. 7 (73) (1962) 45–58.
[63] J.D. Eshelby, F.C. Frank, F.R.N. Nabarro, XLI The equilibrium of linear arrays of dislocations, Lond. Edinburgh Dublin Philos. Mag. J. Sci. 42 (327) (1951) 351–364.
[64] T. Benjamin Britton, A.J. Wilkinson, Stress fields and geometrically necessary dislocation density distributions near the head of a blocked slip band, Acta Mater. 60 (16) (2012) 5773–5782.
[65] R.v. Mises, Mechanik der plastischen Formänderung von Kristallen, ZAMM-J. Appl. Math. Mech. 8 (3) (1928) 161–185.
[66] Y. Zhu, X. Wu, Perspective on hetero-deformation induced (HDI) hardening and back stress, Mater. Res. Lett. 7 (10) (2019) 393–398.
[67] T.H. Chou, W.P. Li, H.W. Chang, X.H. Du, W.S. Chuang, T. Yang, Y.T. Zhu, J. C. Huang, Quantitative analysis of hetero-deformation induced strengthening in heterogeneous grain structure, Int. J. Plast. 159 (2022), 103482.
[68] C.S. Pande, M.E.M. Pozner, P.M. Hazzledine, Interaction between dislocation pile ups, J. Appl. Phys. 43 (7) (1972) 2931–2936.
[69] P. Streitenberger, J.F. Knott, On the calculation of moments of dislocation pile-ups from the stress intensity factor, Philos. Mag. A 75 (2) (1997) 469–483.
[70] W.A. Soer, K.E. Aifantis, J.T.M. De Hosson, Incipient plasticity during nanoindentation at grain boundaries in body-centered cubic metals, Acta Mater. 53 (17) (2005) 4665–4676.
[71] A. Akhtar, Basal slip and twinning in α-titanium single crystals, Metall. Trans. A 6 (5) (1975) 1105–1113.
[72] L. Bao, C. Schuman, J.S. Lecomte, M.J. Philippe, X. Zhao, C. Esling, A study of twin variant selection and twin growth in titanium, Adv. Eng. Mater. 13 (10) (2011) 928–932.
[73] S. Wang, C. Schuman, L. Bao, J.S. Lecomte, Y. Zhang, J.M. Raulot, M.J. Philippe, X. Zhao, C. Esling, Variant selection criterion for twin variants in titanium alloys deformed by rolling, Acta Mater. 60 (9) (2012) 3912–3919.
[74] F. Siska, L. Stratil, J. Cizek, A. Ghaderi, M. Barnett, Numerical analysis of twin thickening process in magnesium alloys, Acta Mater. 124 (2017) 9–16.
[75] M. Arul Kumar, A.K. Kanjarla, S.R. Niezgoda, R.A. Lebensohn, C.N. Tomé, Numerical study of the stress state of a deformation twin in magnesium, Acta Mater. 84 (2015) 349–358.
[76] B. Leu, M.A. Kumar, P.F. Rottmann, K.J. Hemker, I.J. Beyerlein, Micromechanical fields associated with irregular deformation twins in magnesium, J. Mater. Eng. Perform. (2022).
[77] L.E. Murr, Dislocation ledge sources: dispelling the myth of frank–read source importance, Metall. Mater. Trans. A 47 (12) (2016) 5811–5826.
[78] J.R. Morris†, Y. Ye, M.H. Yoo, First-principles examination of the twin boundary in hcp metals, Philos. Mag. 85 (2–3) (2005) 233–238.
[79] S. Wang, K. Dang, R.J. McCabe, L. Capolungo, C.N. Tomé, Three-dimensional atomic scale characterization of $\{11\bar{2}2\}$ twin boundaries in titanium, Acta Mater. 208 (2021), 116707.
[80] H. El Kadiri, C.D. Barrett, J. Wang, C.N. Tomé, Why are $\{10\bar{1}2\}$ twins profuse in magnesium? Acta Mater. 85 (2015) 354–361.

[81] A. Ostapovets, A. Serra, Review of non-classical features of deformation twinning in hcp metals and their description by disconnection mechanisms, Metals (2020) (Basel).
[82] C.D. Barrett, H. El Kadiri, Fundamentals of mobile tilt grain boundary faceting, Scr. Mater. 84-85 (2014) 15–18.
[83] F. Wang, S.R. Agnew, Dislocation transmutation by tension twinning in magnesium alloy AZ31, Int. J. Plast. 81 (2016) 63–86.
[84] P. Chen, F. Wang, B. Li, Dislocation absorption and transmutation at $\{10\bar{1}2\}$ twin boundaries in deformation of magnesium, Acta Mater. 164 (2019) 440–453.
[85] B.M. Morrow, R.J. McCabe, E.K. Cerreta, C.N. Tomé, Observations of the atomic structure of tensile and compressive twin boundaries and twin–twin interactions in zirconium, Metall. Mater. Trans. A 45 (13) (2014) 5891–5897.
[86] K. Dang, S. Wang, M. Gong, R.J. McCabe, J. Wang, L. Capolungo, Formation and stability of long basal-prismatic facets in Mg, Acta Mater. 185 (2020) 119–128.
[87] C.D. Barrett, H. El Kadiri, The roles of grain boundary dislocations and disclinations in the nucleation of $\{10\bar{1}2\}$ twinning, Acta Mater. 63 (2014) 1–15.
[88] A. Ostapovets, R. Gröger, Twinning disconnections and basal–prismatic twin boundary in magnesium, Modell. Simul. Mater. Sci. Eng. 22 (2) (2014), 025015.